Title: The genetic architecture of human cerebellar morphology supports a key role for the cerebellum in recent human evolution and psychopathology

Authors: Torgeir Moberget[1,2], Dennis van der Meer*[1,3], Shahram Bahrami*[1], Daniel Roelfs[1], Oleksandr Frei[1], Tobias Kaufmann[1,4], Sara Fernandez-Cabello[1], Milin Kim[1], Thomas Wolfers[1,4], Joern Diedrichsen[5], Olav B. Smeland[1], Alexey Shadrin[1], Anders Dale[6], Ole A. Andreassen[1] & Lars T. Westlye[1,7].

*These two authors contributed equally

To whom correspondence should be addressed: Torgeir Moberget, Norwegian Centre for Mental Disorders Research (NORMENT), Division of Mental Health and Addiction, Oslo University Hospital, Oslo, Norway. Email: torgeir.moberget@gmail.com

Affiliations:

1: Norwegian Centre for Mental Disorders Research (NORMENT), Division of Mental Health and Addiction, Oslo University Hospital & Institute of Clinical Medicine, University of Oslo, Oslo, Norway

2: Department of Behavioral Science, School of Health Sciences, Oslo Metropolitan University - OsloMet, Oslo, Norway.

3: School of Mental Health and Neuroscience, Faculty of Health, Medicine and Life Sciences, Maastricht University, The Netherlands

4: Department of Psychiatry and Psychotherapy, Tübingen Center for Mental Health, University of Tübingen, Germany

5: Brain and Mind Institute, University of Western Ontario, London, Canada

6: Center for Multimodal Imaging and Genetics, University of California at San Diego, La Jolla, CA, USA

7: Department of Psychology, Faculty of Social Sciences, University of Oslo, Norway

Contributions: TM originally conceived of the project. TM, DvdM and SB performed the analyses. TM, LTW and OAA wrote the initial draft of the manuscript. All authors discussed the results and contributed to the final manuscript.

Keywords: Cerebellum; structural magnetic resonance imaging (sMRI), Genome-wide association analysis (GWAS), brain evolution, psychopathology

Abstract

The functional domain of the human cerebellum has expanded beyond motor control to also include cognitive and affective functions. In line with this notion, cerebellar volume has increased over recent primate evolution and cerebellar alterations have been linked to heritable mental disorders. In order to map the genetic architecture of human cerebellar morphology, we studied a large imaging genetics sample from the UK Biobank (n discovery = 27,302; n replication: 11,264) with state-of-the art neuroimaging and biostatistics tools. Multivariate GWAS (MOSTest) on empirically derived regional cerebellar MRI features yielded 351 significant genetic loci (228 novel, 94% replicated) showing both shared and specific effects across regions. Gene level analyses revealed enrichment for genes associated with human-specific evolution over the last ~6-8 million years, to a similar or higher degree than cerebral comparison phenotypes. We also observed genetic overlap between cerebellar morphology and major mental disorders, supporting cerebellar involvement in psychopathology.

Introduction

The cerebellum contains ~80% of all neurons in the human brain[1] and has rapidly expanded in volume over recent primate evolution[2]. Indeed, the surface area of the cerebellar cortex extends to almost 80% of the surface area of the cerebral cortex[3]. Comparative genetic analyses suggest that protein coding genes with known roles in cerebellar development have been subject to a similar, or even greater, rate of hominid evolution as compared to cerebro-cortical developmental genes[4]. Thus, the evolution of the cerebellum may have played a key role in the emergence of human cognition, including language[5].

A growing number of neuroimaging and clinical studies in humans also link cerebellar structure and function to a wide range of cognitive and affective functions[6-8], as well as to a number of heritable developmental[9] and psychiatric[10] disorders where these abilities either fail to develop properly or are compromised later in life. However, compared to supra-tentorial brain structures such as the cerebral cortex[11] and the hippocampus[12], few studies have mapped the genetic architecture of the cerebellum.

Of note, the few existing cerebellar genome-wide association studies (GWAS) have mostly been restricted to total cerebellar volume[13,14], thus largely ignoring regional variation in cerebellar morphology. Importantly, such variation in the relative volumes of cerebellar subregions (i.e., variation in cerebellar shape independent of total cerebellar volume) has been associated with variation in behavioral repertoires in several species[15,16], including domain-general cognition in primates[16].

We here performed a GWAS of MRI-derived regional cerebellar morphological features in a large population-based sample from the UK biobank (n discovery = 27,302; n replication:11,264), functionally characterized the genetic signal, tested for enrichment of genes linked to human evolution and assessed genetic overlap with major mental disorders.

Results

Data-driven decomposition of cerebellar grey matter maps reveals highly reproducible morphological features.

Since traditional atlases of the cerebellar cortex based on gross anatomical landmarks only partially overlap with more recent functional parcellations of the cerebellum[17-25], we first used a data-driven approach (non-negative matrix factorization, NNMF[26-28]) to parcellate voxel-based morphometry (VBM) based maps of cerebellar grey matter volume from 28,212 participants into robustly reproducible sub-regions. NNMF yielded highly reproducible decompositions (across split-half datasets) for model orders (i.e., number of components specified) ranging from 2 to 100 (see Online Methods for details about the study sample, MRI processing and quality control procedures). After observing that the improved fit to the original data seen with higher model orders tended to level off

between 15 and 30 components (indicating that the intrinsic dimensionality of the data might have been reached), we decided on a model order of 23 based on its good split-half reproducibility (see Fig. 1b, Online Methods for details regarding model order selection, as well as Supplementary Figure 1 for summary maps of all tested model orders).

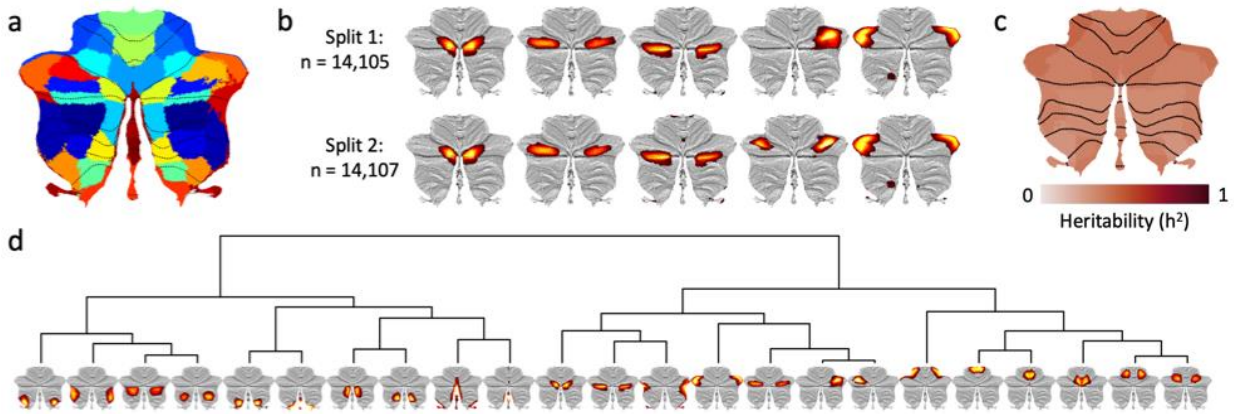

Figure 1: Data driven decomposition of cerebellar grey matter maps yields highly reproducible and moderately heritable morphological features. *a: Binarized winner-takes-all map for the 23-component solution based on data-driven decomposition of cerebellar grey matter maps from 28,212 participants. Note that empirically derived boundaries between cerebellar regions only partially follow traditional lobular borders (marked with dotted black lines); b: Five distinct components overlapping cerebellar Crus I derived from the split-half reliability analyses. While one of these components emerged as bilateral in Split 2, the remaining four components were almost identical, despite being derived from two independent samples; c: Narrow sense (SNP-based) heritability of the 23 components (see Supplementary Data 5 for numerical values). d: Hierarchical clustering of the 23 components (derived from the full sample decomposition) based on their pairwise genetic correlations revealed a primary division between the anterior and posterior cerebellum, with additional separations between medial and lateral regions. The full genetic correlation matrix can be found in Supplementary Data 6.*

Of note, our data-driven decomposition differed markedly from the standard cerebellar atlas based on gross anatomical features, shown as dotted lines in Fig 1a (see Supplementary Figure 2 for all 23 components and Supplementary Data 1 for quantification of overlap between NNMF-derived components and standard cerebellar anatomical regions, i.e. lobules). For instance, five distinct components overlapped Crus I of cerebellar lobule VII (shown in Fig 1b), an anatomical region which already started to split into separate components at a model order of three. We further observed only partial overlap with task-based functional parcellations of the cerebellar cortex (Supplementary Data 2). While some components clearly overlapped cerebellar regions previously associated with hand movements, eye-movements/saccades or autobiographical recall, other data-driven components overlapped multiple functionally defined cerebellar regions.

Cerebellar morphological features are heritable and reveals a distinct anterior-posterior pattern based on their bivariate genetic correlations.

After removal of one of each genetically related pair of individuals (n = 910), 27,302 participants remained for the genetic analyses. In addition to the 23 regional cerebellar morphometric features of primary interest, we also included total cerebellar volume, estimated total intracranial volume and 9 cerebral brain phenotypes to serve as covariates and/or comparison phenotypes. Prior to the genetic analyses, all morphological features were adjusted for effects of scanner site, sex, age, estimated total intracranial volume, 40 genetic population components, genetic analysis batch and a quantitative structural MRI quality index (the Euler number[29]) using general additive models, before finally being rank-order normalized (see Online Methods for details).

To validate our analysis approach, we computed genetic correlations (using LD-score regression, LDSC[30]) between univariate GWAS results on the comparison features and previously neuroimaging GWAS studies. Results showed a mean r_g of .90 (range: .80-.99, see Supplementary Data 3). For the 23 cerebellar morphological features, we computed genetic correlations between discovery (n = 27,302) and replication (n = 11,264) samples using LDSC[30]. These genetic correlations were high (mean rG: .92; range: .83-1), indicating reliable genetic signals (see Supplementary Data 4).

Genetic complex trait analysis (GCTA[31]) revealed SNP-based heritability estimates (h^2) ranging from .33 to .44 (all *p*-values<2e-89, Figure 1c and Supplementary Data 5). Analyses of total cerebellar volume (h^2 = .35), estimated total intracranial volume (h^2 = .41) and the 9 cerebral comparison phenotypes (h^2 range: .26 to .45) gave a similar range of heritability estimates (Supplementary Data 5).

Hierarchical clustering of cerebellar features based on their bivariate genetic correlation matrix (GCTA-based rG ranging from 0.35 to 0.98, Supplementary Data 6) revealed a primary anterior-posterior division running along the horizontal fissure separating Crus I and Crus II, with secondary divisions grouping features into more lateral or medial, as well as more anterior and posterior features within the major anterior and posterior regions (Fig 1d). Of note, the primary division along the horizontal fissure was also evident from the (genetically naïve) two-component NNMF decomposition, while medial-to-lateral divisions already began to emerge with a model order of three (see Supplementary Figure 1).

In order to examine whether this phenotypic and genetic correlation structure was also reflected in regional cerebellar gene expression patterns, we used the abagen toolbox[32] to extract Allen Human Brain Atlas[33] gene expression profiles for 22 of the 23 morphological features and computed their bivariate Pearson correlations (across 15,631 genes; Supplementary Data 7) and hierarchical clustering solution (Supplementary Figure 4). The anterior-posterior boundary across the horizontal fissure was also evident in the gene expression data, which in addition highlighted distinct gene expression patterns for the posterior midline (grouped together with the horizontal fissure), as well as for the most lateral regions of the cerebellar cortex.

Multivariate GWAS reveals 351 genetic loci associated with cerebellar morphology. Figure 2a shows the main results for the multivariate GWAS across the 23 cerebellar morphological features applying MOSTest[34]. We observed 35,098 genome-wide significant (GWS) SNPs, which were mapped by FUMA[35] to a total of 51,803 candidate SNPs by adding reference panel SNPs in high LD (r >.6) with GWS SNPs. The 51,803 candidate SNPs were represented by 1,936 independent significant SNPs and 560 lead SNPs in 351 genomic loci (see Supplementary Data 8). The QQ-plot of the MOSTest results did not suggest inflation, while the QQ-plot of results based on permuted data (under the null hypothesis) confirmed the validity of the MOSTest analytical approach (Supplementary Figure 5).

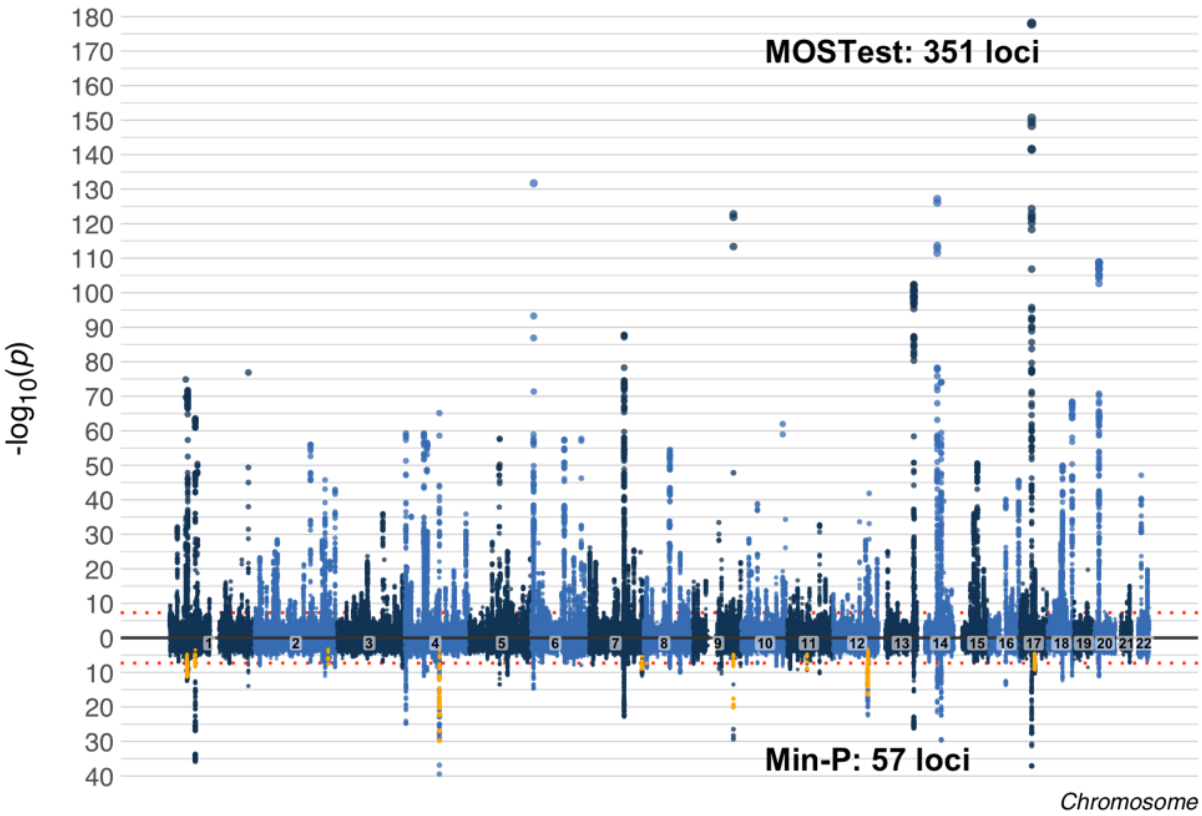

Figure 2: Multivariate GWA analysis of the 23 cerebellar morphological features revealed 351 independent genome-wide significant (GWS) loci. *The upper half of the Miami plot shows the main results from the multivariate analysis. For comparison, the lower half displays results from a series of 23 univariate analyses (yielding 57 loci corrected for multiple comparisons using the standard min-P approach), as well as results from a univariate analysis of total cerebellar grey matter (yielding 10 loci) marked in orange.*

Annotation of all candidate SNPs using ANNOVAR[36] as implemented in FUMA[35] revealed that the majority of candidate SNPs were intronic (57.8%) or intergenic (38.3%). While only 0.7% were exonic, about 81% of the candidate SNPs were assigned minimal chromatin states between 1 and

7 (i.e., open chromatin states), implying effects on active transcription[37] (see Supplementary Data 9-10).

We evaluated the robustness of these multivariate results using a multivariate replication procedure established in Loughnan et al[37], which computes a composite score from the mass-univariate *z*-statistics (i.e., applying multivariate weights from the discovery sample to the replication sample input data) and then tests for associations between this composite score and genotypes in the replication sample (for mathematical formulation see Loughnan et al[37]). Results showed that 97% of loci lead SNPs present in both samples replicated at a nominal significance threshold of $p < .05$ (Supplementary Figure 6), and that 74% remained significant after Bonferroni correction for the 339 replication tests conducted (Figure 2b and Supplementary Data 8). Moreover, 99% of loci lead SNPs showed the same effect direction across discovery and replication samples (Supplementary Figure 6 and Supplementary Data 8). Thus, 329 (94%) of the 351 reported loci were replicated.

In addition, we assessed the robustness of the multivariate patterns by computing bivariate correlations between feature z-score vectors assigned to the discovery sample lead SNPs in an independent multivariate GWAS (MOSTest) performed on the replication sample. These correlations (restricted to the 339 loci lead SNPs present in both samples) were relatively high (mean r: .70, see Supplementary Data 8 and Supplementary Figure 7). Figure 3 and Supplementary Figure 7 give some examples of discovery and replication sample multivariate patterns projected back onto the cerebellar cortex.

To compare our main multivariate MOSTest results to univariate approaches, the lower part of the Miami plot (Figure 2a) displays results from a set of univariate GWASs on the cerebellar morphological features (which yielded 57 genomic loci, corrected for multiple comparisons using the min-P approach[38,39], as well as the 10 significant loci resulting from the univariate GWAS on total cerebellar grey matter volume (marked in orange). 52 of the 57 loci identified in the univariate analyses of regional cerebellar features overlapped 55 of the 351 loci identified using the multivariate method, while 9 out of 10 loci identified in the univariate analysis of total cerebellar volume were also identified in the multivariate analysis. Thus, our multivariate analysis of regional cerebellar features increased the yield ~35-fold relative to analyzing total cerebellar volume and ~6-fold relative to performing a set of univariate analyses on the same regional features.

We next compared the current findings with previously reported genetic loci for cerebellar morphology by extracting summary statistics from two recent GWAS studies using the UKBB sample (n = 19k[40] and 33k[41]) that included cerebellar regional volumes among the full set of analyzed brain imaging-derived phenotypes (101[40] and 3,144[41], respectively), as well as two recent GWASs on total cerebellar volume (n = 33k[13] and 27k[14], respectively). Independent GWS loci were identified in FUMA using the same settings as for our primary analyses and employing a liberal *p*-value threshold of 5e-8 (i.e., not correcting for the total number of brain imaging features analyzed). Results showed that 123 of the 351 identified genomic loci overlapped with loci extracted from these three previous

studies. Thus, 228 of the 351 (i.e., 65%) genetic loci reported here are novel to the literature (see Supplementary Data 11).

Significant genetic variants show heterogeneous effects across the cerebellar cortex, influencing both regional and total volumes.

A major advantage of our multivariate analysis approach is its sensitivity to both highly localized and more generally distributed effects of SNPs on cerebellar morphology. This is illustrated in Figure 3, which displays the 351 loci lead SNPs as a function of both the most extreme individual Z-score across all cerebellar features (e.g, analogous to the strongest "local" effect) and of the mean Z-score across these features (i.e. analogous to the main effect on overall cerebellar volume).

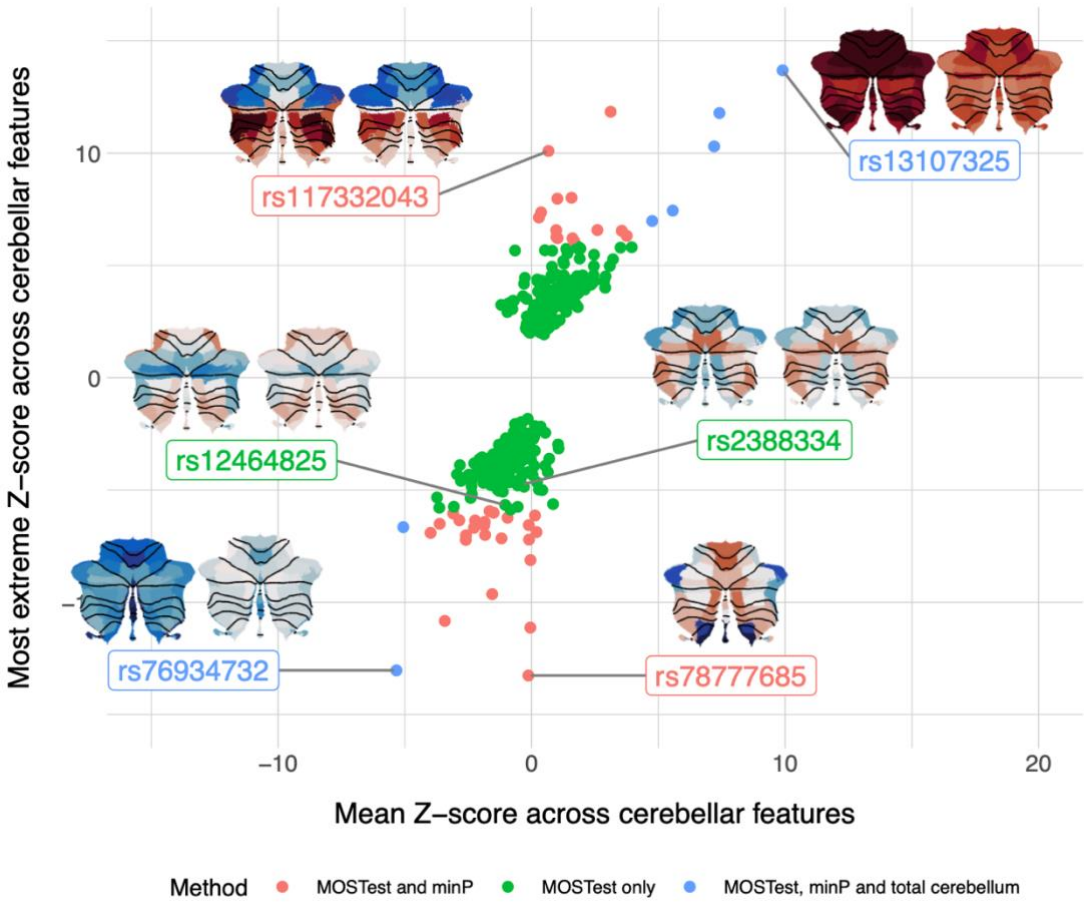

Figure 3: Lead SNPs show spatially heterogeneous – and replicable - effects across the cerebellar cortex. *The 351 loci lead SNPs identified by MOSTest are plotted as a function of main overall effect across all cerebellar features (x-axis: mean Z-score) and most extreme effect for any single cerebellar feature (y-axis: most extreme Z-score across features), and colour coded by SNP discovery method. The cerebellar flat-maps show discovery (left) and replication (right) sample regional distributions of Z-scores (color-scale range from -10 to 10) for a few selected lead SNPs (see Supplementary Data 8 for individual feature Z-scores for all 351 discovery sample loci lead SNPs). SNP rs7877685 was only present in the discovery sample.*

As can be seen, some lead SNPs (e.g. rs13107325; rs76934732) show pronounced positive or negative mean z-scores, indicating a relatively consistent direction of effect across cerebellar features. See also inset figures displaying feature Z-scores projected back onto the cerebellar cortex. Many of these SNPs also emerged in the univariate analysis of total cerebellar volume and were recently reported in GWASs on total cerebellar volume[13,14].

Many other lead SNPs, however, show strong "local" signals with opposite effect directions across features, yielding very weak global signals (e.g. rs117332043; rs78777685). Thus, while several of the most significant SNPs in this category have previously been reported in GWASs including local cerebellar morphological features[40,41], they did not emerge from analyses of total cerebellar volume, neither in the current nor in previous studies.

Finally, our multivariate MOSTest approach is also sensitive to SNPs displaying weaker effects distributed across several cerebellar features, often with opposite effect directions (e.g. rs12464825; rs2388334). For this category of SNPs, neither of the univariate methods have sufficient power at the current sample size. In contrast, these two example SNPs robustly emerged from the multivariate analysis (discovery sample p-values < 1e-56; replication sample p-values <1e-15).

Genes associated with cerebellar morphology show selective expression in cerebellar and prenatal brain tissue, as well as enrichment for genes linked to human accelerated regions.

To functionally characterize the multivariate GWAS signal, we mapped the full set of GWAS p-values to 19,329 protein coding genes using MAGMA[42] and used the resulting gene-level p-values to test for 1) GWS genes, 2) gene expression in brain tissue; and 3) enrichment for genes linked to human accelerated regions (HARs), i.e. sections of DNA that have remained relatively conserved throughout mammalian evolution, before being subject to a burst of changes in humans since divergence of humans from chimpanzees[43,44]. These analyses yielded a total of 534 GWS genes (i.e., 2.78% of all protein coding genes, see Figure 4a and Supplementary Data 11). Using the full set of 19,329 gene-level p-values in MAGMA gene property analyses revealed significant and specific gene expression in cerebellar and prenatal brain tissue (Figure 4b-c, and Supplementary Data 12-13), with the selective cerebellar expression seen in two independent datasets (Allen Human Brain Atlas[33] and The Genotype-Tissue Expression (GTEx) Project).

The MAGMA gene set analysis of HAR-linked genes revealed significant enrichment (p = 7.09e-08) for genes associated with cerebellar morphology (Figure 4d, Supplementary Data 14). Of note, running this same HAR gene set analysis on summary statistics from recent multivariate GWAS studies on cerebrocortical[45] or hippocampal[46] morphological features yielded similar (for cortical features) or significantly weaker (hippocampal features) enrichment effects (Figure 4d, see Online Methods for processing pipeline).

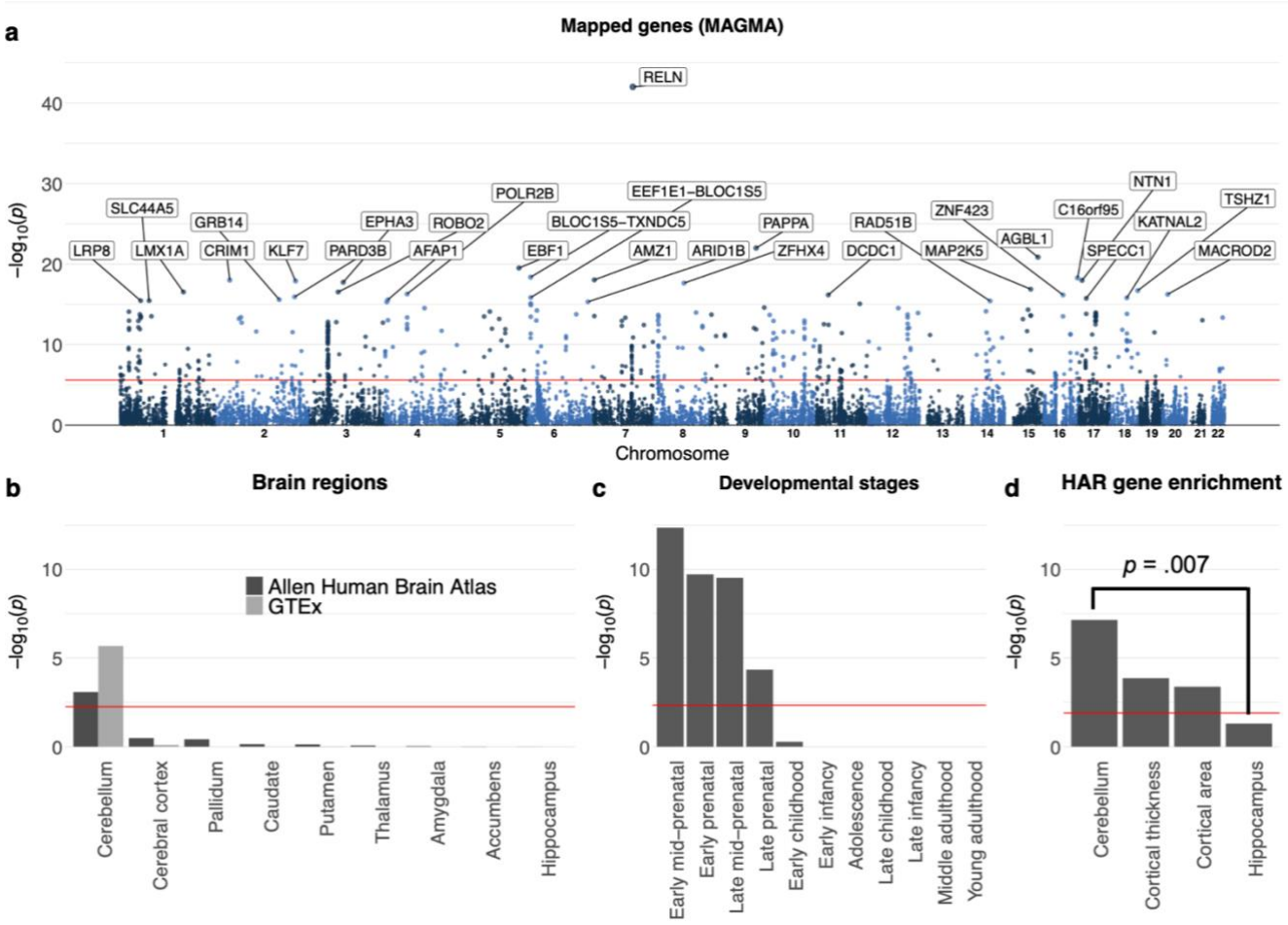

Figure 4: Gene mapping reveals selective enrichment for cerebellar and prenatal brain tissue, as well as for genes linked to human accelerated regions. a: *MAGMA mapped the full range of SNPs from the multivariate GWAS to 19.329 protein-coding genes, 534 of which were genome-wide significant (Bonferroni corrected threshold marked with red line), with the 30 most significant genes labeled in the gene-based Manhattan plot.* ***b-c:*** *MAGMA gene-property analyses revealed selective brain expression in the cerebellum and during prenatal developmental stages.* ***d:*** *MAGMA gene-set analysis revealed significant enrichment for sets of genes previously linked to human accelerated regions (HARs). Figure 4d also shows results from comparative analyses using summary statistics from other multivariate GWASs of MRI-based brain. Red lines mark the Bonferroni-corrected significance threshold for each subplot. See Supplementary Data 11-14 for full results.*

Genes linked to human cerebellar morphology show enrichment for gene sets linked to selective cerebellar gene expression, altered cerebellar morphology in mouse models, human clinical/anthropometric traits, as well as specific biological processes and pathways. In line with the continuous brain tissue gene expression results described above, we also observed significant and relatively selective enrichment for smaller curated sets of genes previously found to be highly and selectively expressed in mouse (Figure 5a, Supplementary Data 15) and human (Figure 5c, Supplementary Data 17) cerebellar brain tissue, as well as for sets of genes previously shown to affect cerebellar morphology in mouse gene perturbation experiments (Figure 5b,

Supplementary Data 16) and various clinical conditions and anthropometric traits in humans (Figure 5d, Supplementary Data 18). The most significant gene ontology and curated gene sets from the MSigDB[47,48] database were related to brain development (e.g., neurogenesis, axon guidance and neuron differentiation, Figure 5e, Supplementary Data 19), and highlighted the reelin signaling pathway (Figure 5f, Supplementary Data 20).

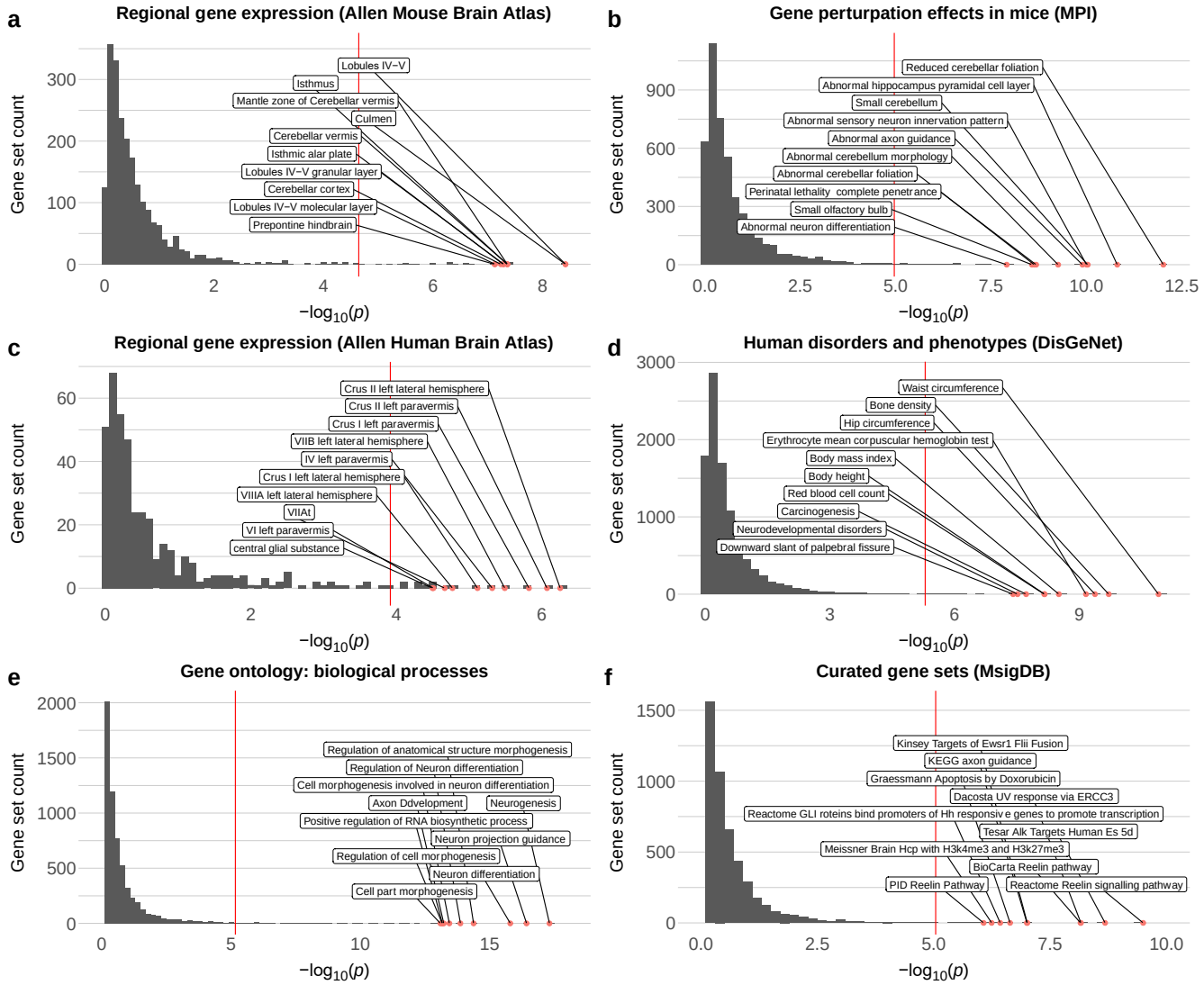

Figure 5: Gene mapping reveals selective enrichment across brain tissues and curated gene sets *MAGMA gene-set analyses revealed significant enrichment for sets of genes previously linked to preferential expression in human* ***(a)*** *and mouse* ***(c)*** *cerebellar tissue, as well as effects on cerebellar morphology (and other brain phenotypes) in mouse gene perturbation experiments* ***(b)*** *and human clinical disorders and phenotypes* ***(d).*** *Significant gene ontology terms were related to neural development* ***(e)****, while curated gene sets highlighted the Reelin signaling pathway* ***(f)****. Across all subplots the x-axis shows the -log10 p-value, the y-axis marks the number of gene sets, and the top 10 most significant gene-sets are labelled. Red lines mark the Bonferroni-corrected significance threshold for each subplot. See Supplementary Data 15-20 for full results.*

As can be seen in Figure 4a (and Supplementary Data 12), *RELN* (encoding the protein Reelin) was also the most significant gene mapped by MAGMA. See also Supplementary Figure 8 for a regional locus plot showing the 12 lead SNPs mapped to *RELN* and their associated z-score maps.

Gene mapping reveals sets of plausible causal genes

In addition to the gene-based mapping strategy using all SNPs described above (MAGMA), we also mapped candidate SNPs to genes using two complementary gene mapping strategies: 1) positional mapping of deleterious SNPs (defined as having a CADD-score[49] > 12.37); and 2) mapping of SNPs previously shown to affect gene expression in cerebellar tissues (i.e., eQTL mapping). Across all three strategies, we mapped a total of 674 unique genes; 531 using MAGMA, 310 using positional and 197 using eQTL mapping (see Figure 6a and Supplementary Data 21).

298 genes were identified by at least two strategies, while 65 genes were mapped by all three strategies. Out of these 674 genes, 61 have previously been associated with cerebellar pathology in humans and/or altered cerebellar morphology in mouse gene perturbation experiments, while 121 have been linked to human accelerated regions (Supplementary Data 21).

Results from gene set analyses on these 674 mapped genes (Figure 6, Supplementary Data 22-27) largely mirrored results from the MAGMA analyses described above, but in addition revealed that this set of 674 mapped genes was also enriched for gene sets associated with several complex clinical phenotypes and anthropometric traits in humans, including cognitive ability, neuroticism and schizophrenia (Supplementary Data 26).

Of note, while the full set of mapped genes showed significant enrichment for sets of genes known to alter cerebellar morphology in mouse mutation or knock-down experiments (Supplementary Data 24), we also note that 613 of the 674 mapped genes have not to our knowledge previously been linked to cerebellar development, anatomy or pathology in mice or humans (Supplementary Data 21), and thus constitute potential targets for future gene perturbation experiments in animal models.

Restricting the above analyses to the 298 genes mapped across at least two strategies did not markedly affect the results (Supplementary Data 22-27, final columns).

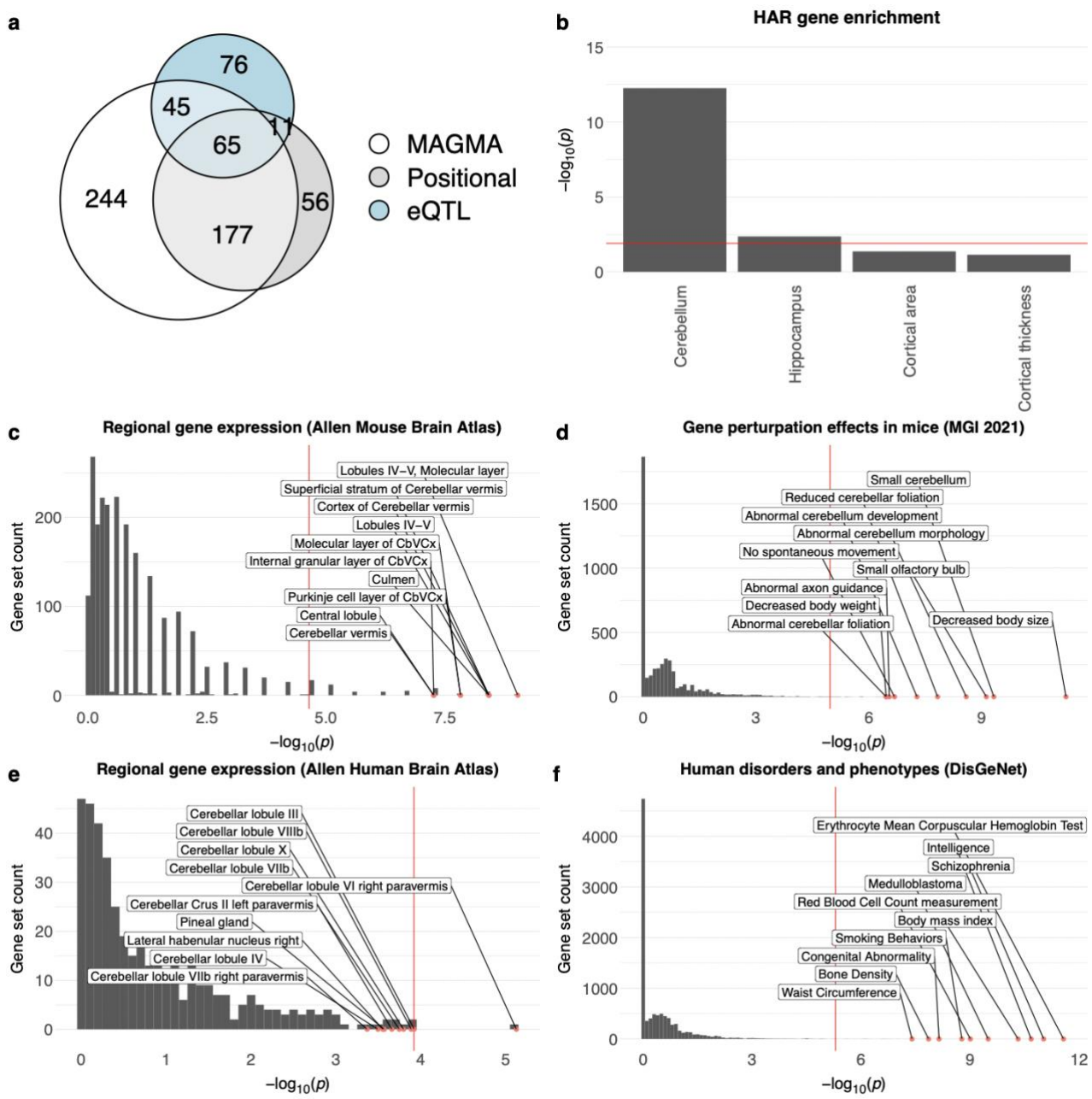

Figure 6: Mapping and functional characterization of plausible causal genes. *The 674 plausible causal genes mapped using three complementary strategies* ***(a)*** *show significant enrichment for sets of genes linked to human accelerated regions* ***(b)****; selective expression in the cerebellum in mice* ***(d)*** *and humans* ***(e)****, as well as effects on cerebellar morphology in mouse gene perturbation studies* ***(d)*** *and human disorders and anthropometric phenotypes* ***(f)****. See Supplementary Data 22-26 for full results.*

Cerebellar morphology shows significant genetic overlap with psychiatric disorders

We finally tested for overlap between the multivariate genetic profile for cerebellar morphology and genetic profiles for five major developmental/psychiatric disorders (attention deficit hyperactivity disorder: ADHD; autism spectrum disorder: ASD; bipolar disorder: BIP; major depressive disorder: MDD; and schizophrenia: SCZ) using conditional/conjunctional FDR analysis[50]. As can be seen in

the conditional QQ-plots in Figure 7, these analyses revealed clear patterns of enriched association with the clinical phenotypes when selecting subsets of SNPs with increasingly stronger association with cerebellar morphology (Fig. 7a and figure insets in 7c-f).

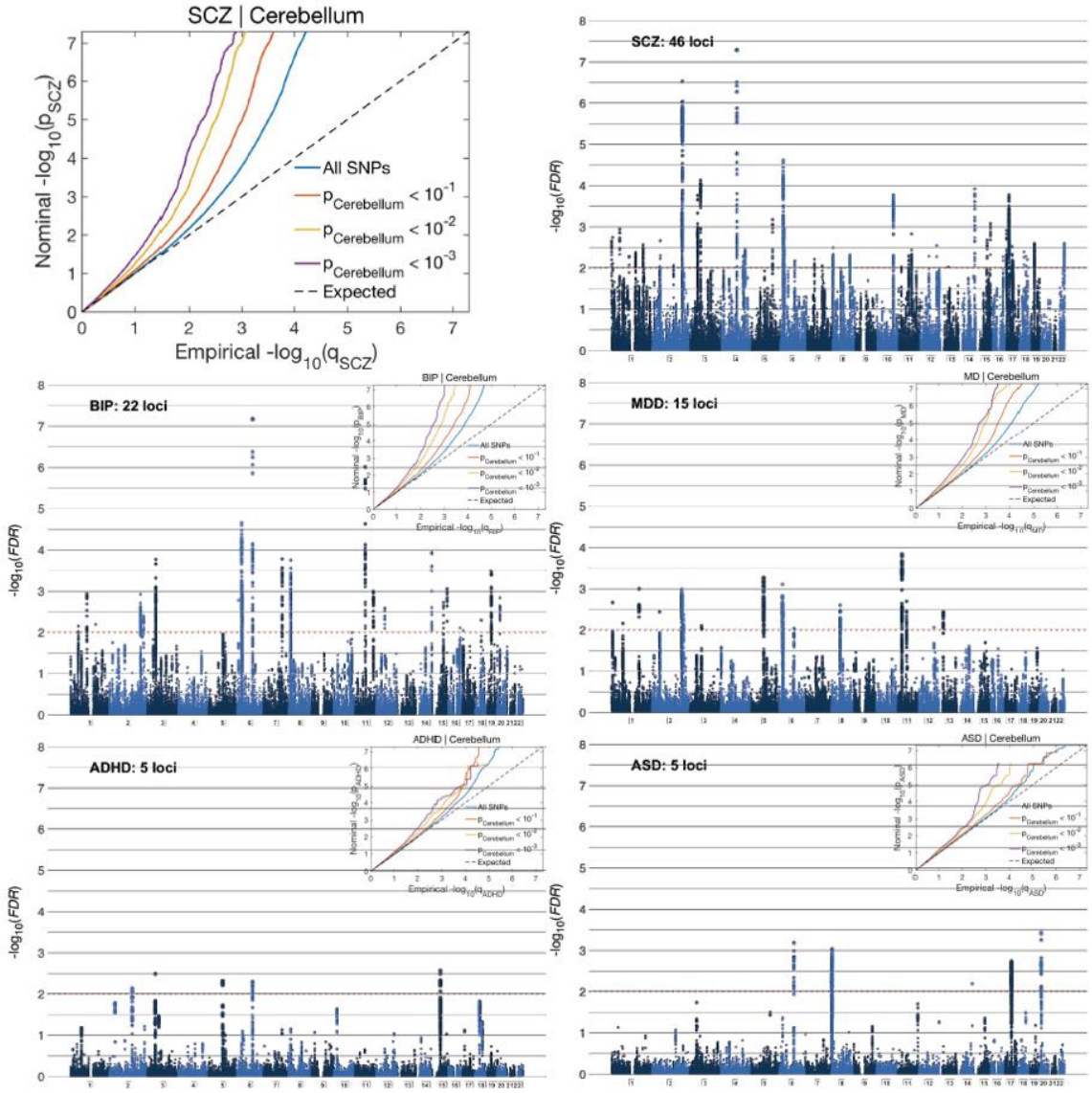

Figure 7: Genetic variants influencing cerebellar morphology overlap with variants associated with five major mental disorders. *Conditional QQ plots plots (top left figure and top right figure insets) show an incremental incidence of association with five mental disorders (leftward deflection) as a function of the significance of association with cerebellar morphology. Manhattan plots show SNPs with significant association with both traits, thresholded at a conjunctional FDR threshold of p > .01 (red dotted line). SCZ: Schizophrenia; BIP: Bipolar Disorder; MDD: Major Depressive Disorder; ADHD: Attention Deficit Hyperactivity Disorder; ASD: Autism Spectrum Disorders.*

See also Supplementary Figure 9 for QQ-plots depicting the reverse association, i.e., enriched association with cerebellar morphology when conditioning on the association with

developmental/psychiatric disorders.Specific genetic variants jointly influencing the two phenotypes were identified using conjunctional FDR analyses at a conservative statistical threshold of p<.01. Results revealed shared genetic loci with all disorders; namely 48 with SCZ, 22 with BIP, 15 with MDD, 5 with ADHD and 5 with ASD (Figure 6; Supplementary Data 28-32). We mapped lead and candidate SNPs for each of these loci to genes using positional and eQTL mapping and checked for gene overlap across disorders (Supplementary Data 33). Of note, the *LRP8* gene (a HAR-linked gene[43,44] encoding a Reelin receptor) emerged from the conjunctional FDR analyses of both BIP and SCZ, thus again highlighting the Reelin signaling pathway.

To complement these multivariate analyses, we also conducted a set of univariate analyses, using LD-score regression[30] to calculate the genetic correlations between each individual cerebellar feature and the five developmental/psychiatric disorders.

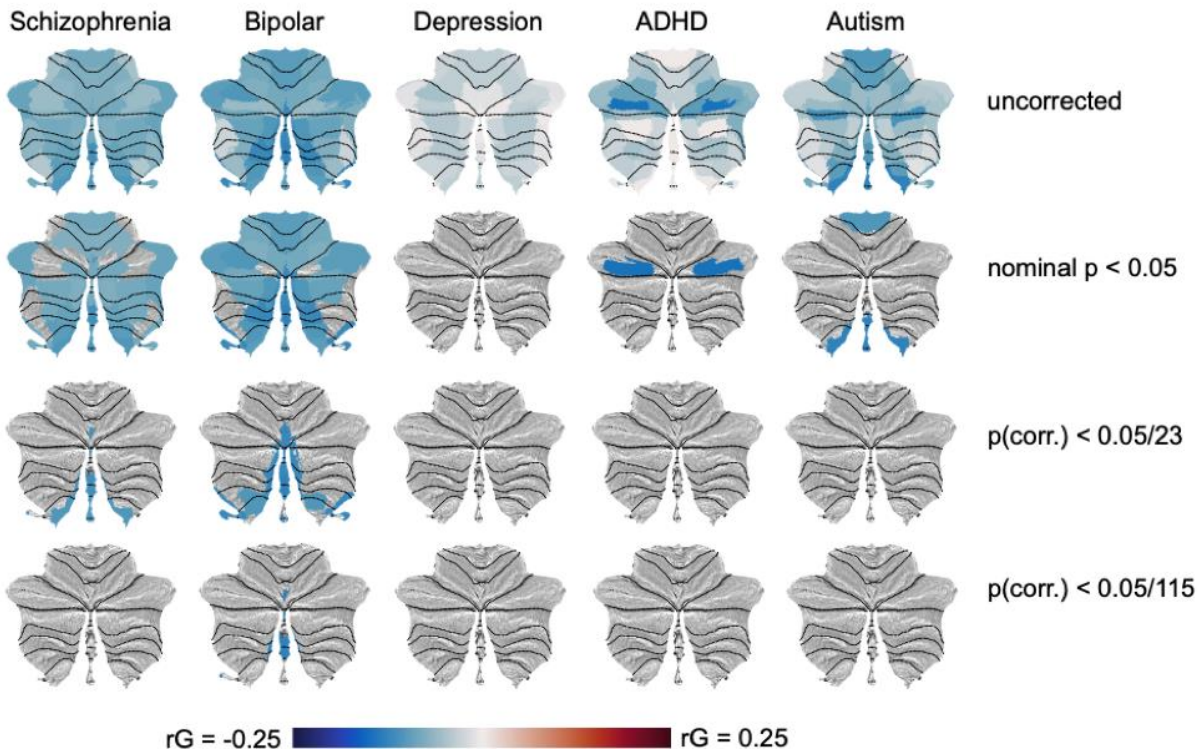

Figure 8: Univariate genetic correlations between cerebellar morphological features and five major mental disorders are negative. *The top row display unthresholded genetic correlations, while these are filtered at increasingly strict statistical thresholds in the following rows, i.e. nominal p-value < .05 (second row); Bonferroni correction for the 23 cerebellar features tested (third row); and Bonferroni correction for both 23 features and 5 clinical conditions (bottom row).*

As can be seen in the first row of Figure 8 (and Supplementary Data 34), genetic correlations with cerebellar morphological features were predominantly negative across diagnoses, indicating that genetic variants associated with a clinical diagnosis tended to also be associated with reduced cerebellar volumes (with 39 out of 115 tested associations showing nominally significant negative correlations; Fig 8, second row). However, all univariate genetic correlations were relatively weak,

and only a few negative genetic correlations with BIP and SCZ survived Bonferroni correction for the 23 features tested. When also correcting for the five clinical conditions, only the negative correlation between BIP and cerebellar feature 23 (primarily overlapping vermal lobules VIIIa and VIIIb) remained significant.

Supplementary Data 35 show genetic correlations between the five disorders and the ten comparison brain phenotypes, as well as total cerebellar volume. In general agreement with the observed pattern for regional cerebellar features, total cerebellar grey matter volume () showed nominally significant negative correlations with BIP (rg: -.10; p = 0.0052) and SCZ (rg: -.09; p = 0.0133). Pallidal volume also showed nominally negative genetic correlations with these two disorders (BIP: rg: -.10; p = 0.0087; SCZ: rg: -.08; p = 0.0172, while ADHD displayed negative genetic correlations with estimated total intracranial volume (rg: -.15; p = 0.0003) and total cortical surface area (rg:-.14 ; p = 0.0065) as well as a positive genetic correlation with hippocampal volume (rg: .13; p = 0.0164). Finally, MDD showed nominally significant negative genetic correlations with volumes of the hippocampus (rg -.08: p = 0.0353) and thalamus (rg: -.09; p = 0.0273). Only the negative genetic correlation between ADHD and estimated total intracranial volume survived Bonferroni correction across the 55 tests performed.

Discussion

The current study identified novel features of the genetic architecture of cerebellar morphology, supported the notion of recent changes over human evolution, implicated specific neurobiological pathways, and demonstrated genetic overlap with major mental disorders.

Our multivariate GWAS using MOSTest identified 351 independent GWS loci associated with cerebellar morphology, increasing the yield ~35-fold relative to analyzing total cerebellar volume and ~6-fold relative to performing a set of univariate analyses on the same regional features in our current sample. 329 (94%) loci from the multivariate analyses were replicated in an independent sample, indicating robust results. After applying a liberal threshold to summary statistics from previous well-powered studies, we find that 228 (65%) of our reported loci are novel. Importantly, among the genes mapped to these novel loci we find several that are known to play important roles in cerebellar development in mice (e.g., *RORA*[51], *FGF8*[52] and *BAHRL1*[53], see Supplementary Data 22).

Results from the current study also bolster the notion of relatively recent changes in cerebellar morphology over human evolution[2,4,15,16] by demonstrating that genes associated with inter-individual variation in cerebellar morphology are enriched for genes linked to human accelerated regions (HARs)[43] of the genome. HARs denote previously conserved regions of the genome that were subject to a burst of changes in humans after divergence of humans from chimpanzees about 6-8 million years ago[43]. Thus, our results suggest that genetic variants influencing cerebellar morphology in modern humans have been subject to selection over relatively recent human evolution, and that cerebellar changes may have played a central part in the

emergence of uniquely human cognitive abilities. Of note, a recent GWAS on total cerebellar volume found no enrichment for HAR-linked genes[14], suggesting that regional cerebellar differences are largely driving this effect. While the comparison with cerebral features should be interpreted with care since different image preprocessing pipelines were employed, it is nonetheless striking that HAR gene enrichment was nominally stronger for cerebellar morphology than for cerebrocortical thickness and area, and significantly stronger than for hippocampal volumes (Figure 4d).

Results from the MAGMA gene property and gene set analyses further show 1) selective gene expression in human cerebellar brain tissue across two independent datasets (Allen Human Brain Atlas and GTEx.8) and significant enrichment for sets of genes which have previously been shown to 2) affect cerebellar morphology in mouse gene perturbation experiments and 3) play key roles in neurodevelopment (e.g., neurogenesis & axon guidance). Further supporting a developmental origin of genetically determined effects on adult cerebellar morphology, the multivariate genetic signal also showed preferential expression in prenatal brain tissue. Our MAGMA enrichment analysis of curated gene sets strongly implicated the Reelin signaling pathway. Indeed, both the gene coding for the Reelin protein (*RELN*) and genes coding for its two receptors (*LRP8* & *VLDLR*) were identified across at least two gene mapping strategies, with *RELN* emerging as the single most significant gene by MAGMA. The Reelin pathway is known to play important roles in neurodevelopment (e.g. neuronal migration), and mutations in the *RELN* and VLDLR[54] (and to a lesser extent LRP8; also known as ApoER2[55]) have been associated with cerebellar malformations and/or dysfunction. LRP8 is also among the genes linked to human accelerated regions (HARs) of the genome.

The sets of genes mapped by the three complementary mapping strategies provide a database for future studies investigating the genetic architecture of cerebellar morphology. For instance, we mapped 616 genes associated with inter-individual variability in human cerebellar morphology that have not yet to our knowledge been examined in mouse gene perturbation experiments and/or associated with cerebellar pathology in humans. Among these, we highlight *MAP2K5* and *GRB14*, two HAR-linked genes mapped across all strategies and associated with lead SNP p-values <1e-50, but whose functions in the brain are largely unknown.

The reported results for previously discovered variants, loci and genes add important information regarding regional effects on cerebellar morphology. For instance, while genetic variants linked to the *RELN* gene have previously been associated with volumes of cerebellar vermal lobules VI-X and hemispheric lobule IX[40,41], we here mapped 12 lead SNPs to *RELN* showing heterogeneous effects across the entire cerebellar cortex (but with peak effects overlapping previously described midline and posterior cerebellar regions, see Supplementary Figure 8).

The observed genetic overlap between cerebellar morphology and the five mental disorders reinforces the recent notion of the cerebellum as a key brain structure in complex clinical traits and disorders[6-10]. Across the five diagnoses, the strongest evidence for genetic overlap with cerebellar morphology was found for SCZ and BIP, likely at least in part due to the fact that these disorder

GWASs were relatively well-powered. While an in-depth discussion of genetic loci jointly influencing psychiatric disorders and cerebellar morphology is beyond the scope of this report, we note that the Reelin pathway again emerges in the genetic overlap analyses for SCZ and BIP. Specifically, the current finding of *LRP8* (a reelin receptor, and HAR-linked gene) as one of the genes jointly associated with cerebellar morphology and the aforementioned severe mental disorders points towards a potential molecular pathway involved in the cerebellar abnormalities previously reported in SCZ[10,56,57] and BIP[56,57]. Indeed, in line with its key importance for brain development and function, the Reelin pathway is also increasingly seen as relevant for a wide range of neurodevelopmental, psychiatric and neurodegenerative disorders[58]. Of particular relevance to the current findings, converging evidence supports LRP8 as a key susceptibility gene for psychosis[59].

Finally, it is worth noting that results from our data-driven decomposition of cerebellar grey matter maps (which was not informed by genetic data), the genetic correlation analyses of the chosen 23-feature solution and gene expression data from the Allen Human Brain Atlas all converge on a similar general pattern of cerebellar morphology. The first boundary to emerge in the data-driven decompositions ran along the horizontal fissure separating Crus I and II of lobule VII, reflecting its centrality in characterizing phenotypic variability in cerebellar morphology at the population level. Of note, this boundary also emerged from clustering of the 23 cerebellar morphological features based on their bivariate genetic correlations or gene expression profiles (based on the Allen Human Brain Atlas). This latter finding essentially mirrors results from a recent report using a different analysis strategy on the same gene expression data[60]. Interestingly, the horizontal fissure has been suggested to mark the border between two separate cerebellar representations of the cerebral cortex, with a possible third representation in lobules IX-X[61]. The current cerebellar results thus complement previous work on the hierarchical genetic organization of the cerebral cortex, which has identified the Rolandic fissure (separating the frontal and parietal lobes) as a main boundary with respect to genetic effects of effects of surface area[62], as well as a superior-inferior gradient for genetic influences on cortical thickness[63]

In conclusion, the current results enhance our understanding of the genetic architecture of human cerebellar morphology, provide supporting evidence for cerebellar morphological changes during the last ~6-8 million years of human evolution, and reinforce the notion of cerebellar involvement in several mental disorders by demonstrating significant genetic overlap.

Data availability

In this study we used brain imaging and genetics data from the UK Biobank [https://www.ukbiobank.ac.uk/], and GWAS summary statistics obtained from the Psychiatric Genomics Consortium [https://www.med.unc.edu/pgc/shared-methods/], and GWAS catalog. The summary statistics for cerebellar morphology derived in this study is available in our github repository [https://github.com/norment/open-science] (will make this public upon acceptance). FUMA results are available online (will make this public upon acceptance).

Code availability

All code and software needed to generate the results is available as part of public resources, specifically FreeSurfer (https://surfer.nmr.mgh.harvard.edu), SUIT (https://github.com/jdiedrichsen/suit), OPNMF (https://github.com/asotiras/brainparts), MOSTest (https://github.com/precimed/mostest), FUMA (https://fuma.ctglab.nl/), MAGMA (https://ctg.cncr.nl/software/magma), abagen (https://github.com/rmarkello/abagen), conjunctional FDR (https://github.com/precimed/pleiofdr/) and LD score regression (https://github.com/bulik/ldsc).

Acknowledgements

The authors were funded by the South-Eastern Norway Regional Health Authority (TM: 2021-040; OAA: 2013-123, 2017-112, 2019-108. LTW: 2014-097, 2015-073, 2016-083), the Research Council of Norway (TK: 276082, 323961. OAA: 213837, 223273, 248778, 273291, 262656, 229129, 283798, 311993. LTW: 204966, 249795, 273345), Norwegian Health Association (SB: 22731), Stiftelsen Kristian Gerhard Jebsen, and the European Research Council (LTW: ERCStG 802998). The funding bodies had no role in the analysis or interpretation of the data; the preparation, review or approval of the manuscript; nor in the decision to submit the manuscript for publication. This work was performed on the Tjeneste for Sensitive Data (TSD) facilities, owned by the University of Oslo, operated and developed by the TSD service group at the University of Oslo, IT-Department (USIT) and on resources provided by UNINETT Sigma2—the National Infrastructure for High Performance Computing and Data Storage in Norway. The research has been conducted using the UK Biobank Resource (access code 27412) and using summary statistics for various brain disorders. We would like to thank the research participants and employees of UK Biobank and the consortia contributing summary statistics for making this work possible.

References

1. Herculano-Houzel, S. *The human advantage : a new understanding of how our brain became remarkable*, xiii, 256 pages (The MIT Press, Cambridge, Massachusetts, 2016).
2. Barton, R.A. & Venditti, C. Rapid Evolution of the Cerebellum in Humans and Other Great Apes. in *Curr. Biol.* (2014).
3. Sereno, M.I. *et al.* The human cerebellum has almost 80% of the surface area of the neocortex. *Proc Natl Acad Sci U S A* **117**, 19538-19543 (2020).
4. Harrison, P.W. & Montgomery, S.H. Genetics of Cerebellar and Neocortical Expansion in Anthropoid Primates: A Comparative Approach. *Brain Behav Evol* **89**, 274-285 (2017).
5. Leiner, H.C., Leiner, A.L. & Dow, R.S. Cognitive and language functions of the human cerebellum. in *Trends in Neurosciences* Vol. 16 444-447 (1993).
6. Strick, P.L., Dum, R.P. & Fiez, J.A. Cerebellum and Nonmotor Function. in *Annu. Rev. Neurosci.* Vol. 32 413-434 (2009).
7. Buckner, R.L. The cerebellum and cognitive function: 25 years of insight from anatomy and neuroimaging. in *Neuron* Vol. 80 807-815 (2013).
8. King, M., Hernandez-Castillo, C.R., Poldrack, R.A., Ivry, R.B. & Diedrichsen, J. Functional boundaries in the human cerebellum revealed by a multi-domain task battery. *Nat Neurosci* **22**, 1371-1378 (2019).
9. Wang, S.S., Kloth, A.D. & Badura, A. The cerebellum, sensitive periods, and autism. *Neuron* **83**, 518-32 (2014).
10. Moberget, T. *et al.* Cerebellar volume and cerebellocerebral structural covariance in schizophrenia: a multisite mega-analysis of 983 patients and 1349 healthy controls. *Mol Psychiatry* **23**, 1512-1520 (2018).
11. Adams, H.H. *et al.* Novel genetic loci underlying human intracranial volume identified through genome-wide association. *Nat Neurosci* **19**, 1569-1582 (2016).
12. van der Meer, D. *et al.* Brain scans from 21,297 individuals reveal the genetic architecture of hippocampal subfield volumes. *Mol Psychiatry* (2018).
13. Chambers, T. *et al.* Genetic common variants associated with cerebellar volume and their overlap with mental disorders: a study on 33,265 individuals from the UK-Biobank. *Mol Psychiatry* **27**, 2282-2290 (2022).
14. Tissink, E. *et al.* Genome-wide association study of cerebellar volume provides insights into heritable mechanisms underlying brain development and mental health. *Commun Biol* **5**, 710 (2022).
15. Macri, S., Savriama, Y., Khan, I. & Di-Poi, N. Comparative analysis of squamate brains unveils multi-level variation in cerebellar architecture associated with locomotor specialization. *Nat Commun* **10**, 5560 (2019).
16. Smaers, J.B., Turner, A.H., Gomez-Robles, A. & Sherwood, C.C. A cerebellar substrate for cognition evolved multiple times independently in mammals. *Elife* **7**(2018).
17. E, K.-H., Chen, S.-H.A., Ho, M.-H.R. & Desmond, J.E. A meta-analysis of cerebellar contributions to higher cognition from PET and fMRI studies. in *Hum Brain Mapp* Vol. 35 593-615 (2014).
18. Stoodley, C.J. & Schmahmann, J.D. Functional topography in the human cerebellum: a meta-analysis of neuroimaging studies. in *NeuroImage* Vol. 44 489-501 (2009).
19. Buckner, R.L., Krienen, F.M., Castellanos, A., Diaz, J.C. & Yeo, B.T.T. The organization of the human cerebellum estimated by intrinsic functional connectivity. in *Journal of Neurophysiology* Vol. 106 2322-2345 (2011).
20. Sang, L. *et al.* Resting-state functional connectivity of the vermal and hemispheric subregions of the cerebellum with both the cerebral cortical networks and subcortical structures. in *NeuroImage* Vol. 61 1213-1225 (Elsevier Inc., 2012).
21. Krienen, F.M. & Buckner, R.L. Segregated fronto-cerebellar circuits revealed by intrinsic functional connectivity. in *Cerebral Cortex* Vol. 19 2485-2497 (2009).
22. Bernard, J.A. *et al.* Resting state cortico-cerebellar functional connectivity networks: a comparison of anatomical and self-organizing map approaches. in *Front Neuroanat* Vol. 6 31 (2012).
23. Kipping, J.A. *et al.* Overlapping and parallel cerebello-cerebral networks contributing to sensorimotor control: an intrinsic functional connectivity study. in *NeuroImage* Vol. 83 837-848 (2013).

24. Wang, C., Kipping, J., Bao, C., Ji, H. & Qiu, A. Cerebellar Functional Parcellation Using Sparse Dictionary Learning Clustering. *Front Neurosci* **10**, 188 (2016).
25. Kipping, J.A., Tuan, T.A., Fortier, M.V. & Qiu, A. Asynchronous Development of Cerebellar, Cerebello-Cortical, and Cortico-Cortical Functional Networks in Infancy, Childhood, and Adulthood. *Cereb Cortex* (2016).
26. Sotiras, A., Resnick, S.M. & Davatzikos, C. Finding imaging patterns of structural covariance via Non-Negative Matrix Factorization. *Neuroimage* **108**, 1-16 (2015).
27. Sotiras, A. *et al.* Patterns of coordinated cortical remodeling during adolescence and their associations with functional specialization and evolutionary expansion. *Proc Natl Acad Sci U S A* **114**, 3527-3532 (2017).
28. Varikuti, D.P. *et al.* Evaluation of non-negative matrix factorization of grey matter in age prediction. *Neuroimage* **173**, 394-410 (2018).
29. Rosen, A.F.G. *et al.* Quantitative assessment of structural image quality. *Neuroimage* **169**, 407-418 (2018).
30. Bulik-Sullivan, B.K. *et al.* LD Score regression distinguishes confounding from polygenicity in genome-wide association studies. *Nat Genet* **47**, 291-5 (2015).
31. Yang, J., Lee, S.H., Goddard, M.E. & Visscher, P.M. GCTA: a tool for genome-wide complex trait analysis. *Am J Hum Genet* **88**, 76-82 (2011).
32. Markello, R.D. *et al.* Standardizing workflows in imaging transcriptomics with the abagen toolbox. *Elife* **10**(2021).
33. Hawrylycz, M.J. *et al.* An anatomically comprehensive atlas of the adult human brain transcriptome. *Nature* **489**, 391-399 (2012).
34. van der Meer, D. *et al.* Understanding the genetic determinants of the brain with MOSTest. *Nat Commun* **11**, 3512 (2020).
35. Watanabe, K., Taskesen, E., van Bochoven, A. & Posthuma, D. Functional mapping and annotation of genetic associations with FUMA. *Nat Commun* **8**, 1826 (2017).
36. Wang, K., Li, M. & Hakonarson, H. ANNOVAR: functional annotation of genetic variants from high-throughput sequencing data. *Nucleic Acids Res* **38**, e164 (2010).
37. Loughnan, R.J. *et al.* Generalization of cortical MOSTest genome-wide associations within and across samples. *Neuroimage* **263**, 119632 (2022).
38. van der Sluis, S., Posthuma, D. & Dolan, C.V. TATES: efficient multivariate genotype-phenotype analysis for genome-wide association studies. *PLoS Genet* **9**, e1003235 (2013).
39. O'Reilly, P.F. *et al.* MultiPhen: joint model of multiple phenotypes can increase discovery in GWAS. *PLoS One* **7**, e34861 (2012).
40. Zhao, B. *et al.* Genome-wide association analysis of 19,629 individuals identifies variants influencing regional brain volumes and refines their genetic co-architecture with cognitive and mental health traits. *Nat Genet* **51**, 1637-1644 (2019).
41. Smith, S.M. *et al.* An expanded set of genome-wide association studies of brain imaging phenotypes in UK Biobank. *Nat Neurosci* **24**, 737-745 (2021).
42. de Leeuw, C.A., Mooij, J.M., Heskes, T. & Posthuma, D. MAGMA: generalized gene-set analysis of GWAS data. *PLoS Comput Biol* **11**, e1004219 (2015).
43. Wei, Y. *et al.* Genetic mapping and evolutionary analysis of human-expanded cognitive networks. *Nat Commun* **10**, 4839 (2019).
44. Won, H., Huang, J., Opland, C.K., Hartl, C.L. & Geschwind, D.H. Human evolved regulatory elements modulate genes involved in cortical expansion and neurodevelopmental disease susceptibility. *Nat Commun* **10**, 2396 (2019).
45. van der Meer, D. *et al.* The genetic architecture of human cortical folding. *Sci Adv* **7**, eabj9446 (2021).
46. Bahrami, S. *et al.* Distributed genetic architecture across the hippocampal formation implies common neuropathology across brain disorders. *Nat Commun* **13**, 3436 (2022).
47. Liberzon, A. *et al.* The Molecular Signatures Database (MSigDB) hallmark gene set collection. *Cell Syst* **1**, 417-425 (2015).
48. Subramanian, A. *et al.* Gene set enrichment analysis: a knowledge-based approach for interpreting genome-wide expression profiles. *Proc Natl Acad Sci U S A* **102**, 15545-50 (2005).
49. Kircher, M. *et al.* A general framework for estimating the relative pathogenicity of human genetic variants. *Nat Genet* **46**, 310-5 (2014).

50. Andreassen, O.A. *et al.* Improved detection of common variants associated with schizophrenia and bipolar disorder using pleiotropy-informed conditional false discovery rate. *PLoS Genet* **9**, e1003455 (2013).
51. Guissart, C. *et al.* Dual Molecular Effects of Dominant RORA Mutations Cause Two Variants of Syndromic Intellectual Disability with Either Autism or Cerebellar Ataxia. *Am J Hum Genet* **102**, 744-759 (2018).
52. Chi, C.L., Martinez, S., Wurst, W. & Martin, G.R. The isthmic organizer signal FGF8 is required for cell survival in the prospective midbrain and cerebellum. *Development* **130**, 2633-44 (2003).
53. Li, S., Qiu, F., Xu, A., Price, S.M. & Xiang, M. Barhl1 regulates migration and survival of cerebellar granule cells by controlling expression of the neurotrophin-3 gene. *J Neurosci* **24**, 3104-14 (2004).
54. Valence, S. *et al.* RELN and VLDLR mutations underlie two distinguishable clinico-radiological phenotypes. *Clin Genet* **90**, 545-549 (2016).
55. Larouche, M., Beffert, U., Herz, J. & Hawkes, R. The Reelin receptors Apoer2 and Vldlr coordinate the patterning of Purkinje cell topography in the developing mouse cerebellum. *PLoS One* **3**, e1653 (2008).
56. Wolfers, T. *et al.* Mapping the Heterogeneous Phenotype of Schizophrenia and Bipolar Disorder Using Normative Models. *JAMA Psychiatry* **75**, 1146-1155 (2018).
57. Wolfers, T. *et al.* Replicating extensive brain structural heterogeneity in individuals with schizophrenia and bipolar disorder. *Hum Brain Mapp* **42**, 2546-2555 (2021).
58. Armstrong, N.C., Anderson, R.C. & McDermott, K.W. Reelin: Diverse roles in central nervous system development, health and disease. *Int J Biochem Cell Biol* **112**, 72-75 (2019).
59. Li, M. *et al.* Convergent Lines of Evidence Support LRP8 as a Susceptibility Gene for Psychosis. *Mol Neurobiol* **53**, 6608-6619 (2016).
60. King, M.Z., Zonglei; Ivry, Richard B.; Weiner, Kevin S. Transcriptomic Gradients Of The Human Cerebellum.
61. Guell, X., Gabrieli, J.D.E. & Schmahmann, J.D. Triple representation of language, working memory, social and emotion processing in the cerebellum: convergent evidence from task and seed-based resting-state fMRI analyses in a single large cohort. *Neuroimage* **172**, 437-449 (2018).
62. Chen, C.H. *et al.* Hierarchical genetic organization of human cortical surface area. *Science* **335**, 1634-6 (2012).
63. Chen, C.H. *et al.* Genetic topography of brain morphology. *Proc Natl Acad Sci U S A* **110**, 17089-94 (2013).

Online Methods:

Participants

For our main analyses, T1-weighted MR images, demographic and genetic data from 39,178 UK Biobank participants were accessed using access number 27412. After removing 1043 participants who either had missing genetic data or had withdrawn consent (as of 19.11.2019), data from 38,135 participants remained for the main analysis (age range: 44.6-82.1; mean age: 64.1, 51.9% female). Following quality control procedures (QC, see below), 28,212 UK Biobank participants of European descent remained for the main analyses (age range: 45.1-82.1; mean age: 64.1, 55.1% female), 910 of which were identified as close relatives and removed prior to genetic analyses (see below), leaving a final sample for the primary analyses of 27,302 (age range: 45.1-82.1; mean age: 64.1, 54.9% female). For the replication sample, we accessed a newer release of UK Biobank participants (n = 48,045) and removed the 27,302 participants included in the primary analyses. After running through identical QC procedures as for the main sample (although applied only to the cerebellar features of primary interest and covariates included when analyzing these), the replication sample consisted of 11,264 unrelated UK Biobank participants of European descent (age range: 46.1-83.7; mean age: 66.8, 46.9% female). The UK Biobank was approved by the National Health Service National Research Ethics Service (ref. 11/NW/0382),

Initial MR image processing

MRI data was first processed using the recon-all pipeline in Freesurfer 5.3[64], yielding a large number of brain features. Of these, we retained measures of estimated total intracranial volume (eTIV), total cerebro-cortical surface area, average cerebro-cortical thickness as well as the volumes of seven subcortical structures (hippocampus, amygdala, thalamus, pallidum, putamen, caudate nucleus and nucleus accumbens) as cerebral (or global, in the case of eTICV) comparison regions for our main cerebellar analyses. These anatomical features were averaged across hemispheres, yielding a total of ten comparison phenotypes.

Next, the bias-field corrected T1-images from the FreeSurfer analyses were analyzed using the cerebellum-optimized SUIT-toolbox[65]. In brief, SUIT isolates the cerebellum and brain stem from T1-images, segments cropped images into grey and white matter, and normalizes these tissue probability maps to a cerebellum-specific anatomical template. After multiplying the grey matter maps with the Jacobian of the transformation matrix (i.e. preserving information about absolute volumes), we extracted grey matter intensity values overlapping the 28 cerebellar lobular labels in the probabilistic SUIT-atlas. Since cerebellar volumetric indices showed high correlations across the two hemispheres (range: .87-.96; mean: .94), we created mean volumetric measures by averaging across hemispheres. Finally, we also combined the two smallest regions in the SUIT-atlas (Vermis Crus I and II located in the midline, average volumes: 2.9 and 293.4 mm^2, respectively) to create a new Vermis Crus region (average volume: 296.2 mm^2). This procedure reduced the 28 cerebellar

lobular volumes to 16 morphological indices. Total cerebellar grey matter volume was defined as the sum of all 28 lobular labels in the SUIT-atlas.

Quality control procedures

After excluding 4,818 UKBB participants of non-European origin, anatomical indices from the remaining 33,317 participants went through an iterative quality control (QC) procedure. First, we excluded 639 subjects with a mean Euler number below -217, indicating poor MRI quality[29], as well as 12 subjects with missing and 90 subjects with zero values for any of the key cerebellar or cerebral brain measures of interest. Next, we used general additive models (GAM, implemented in the R-package "mgcv") in order to model the effects of age (estimated as smooth functions for males and females separately, using cubic splines with 10 knots), sex, and scanner site on estimated total intracranial volume (eTIV) and mean thickness of the cerebral cortex. Specifically, we used the following formula:

GAM_model<-gam(Anatomical feature ~ s(Age, bs = "cs", by = Sex, k = 10) + as.factor(Sex) + as.factor(Scanner), data = UKBB_cerebellum_GWAS, select = TRUE, method = "REML")

Adjusted eTIV and mean cortical thickness indices were then created by reconstructing the data using the intercept and residuals from this model (i.e., removing effects of age, sex and scanner), before identifying and rejecting potential outliers, defined as +/- 3 median absolute deviations (MAD)[66] from the median of these adjusted values. Data from 350 subjects were rejected based on these criteria.

For the remaining cerebral anatomical measures, as well as total cerebellar volume, this procedure was then repeated, with scaled eTIV as an additional predictor. Since previous studies have demonstrated that the relationship between regional brain volumes and intracranial volume is not strictly allometric[67,68], we estimated the effect of eTIV using cubic splines with 10 knots. Specifically, we used the following formula:

GAM_model<-gam(Anatomical feature ~ s(Age, bs = "cs", by = Sex, k = 10) + as.factor(Sex) + as.factor(Scanner) + s(eTIV_scaled, bs = "cs", k = 10), data = UKBB_cerebellum_GWAS, select = TRUE, method = "REML")

In order to be maximally sensitive to outliers in relative cerebellar volumes, we replaced eTIV with total cerebellar volume in the GAM models of cerebellar regions of interest (i.e., SUIT atlas regions), using the following formula:

GAM_model<-gam(Anatomical feature ~ s(Age, bs = "cs", by = Sex, k = 10) + as.factor(Sex) + as.factor(Scanner) + total cerebellar volume, data = UKBB_cerebellum_GWAS, select = TRUE, method = "REML")

Adjusted cerebral and cerebellar indices were then created by reconstructing the data using the intercept and residuals from these models (i.e., removing estimated effects of age, sex and eTIV or total cerebellar volume), before rejecting 1792 participants with potential outlier cerebral indices and 2222 participants with potential outlier cerebellar indices (MAD > +/- 3).

This iterative QC procedure resulted in the rejection of 5,105 (i.e., 15.3%) of the original 33,317 datasets, leaving 28,212 datasets for further analysis.

Non-negative matrix factorization

Cerebellar grey matter maps from 28,212 subjects passing the iterative QC procedure were smoothed with a 4mm full-with-half-maximum gaussian kernel in SPM12[69], concatenated across all subjects and multiplied with a binary mask to isolate voxels located in the cerebellar cortex. This cerebellar cortical mask was constructed by multiplying a binary mask containing all 28 cerebellar lobules of the SUIT-atlas with the thresholded (at a value of 0.1) mean (unsmoothed) grey matter segmentation across all 28,212 participants.

The smoothed, concatenated and masked grey matter maps were then subjected to orthogonal projective non-negative matrix-factorization (OPNMF)[26], in order to derive data-driven parcellations of regional cerebellar grey matter volume.

Non-negative matrix factorization (NNMF) is a blind source separation technique that allows structural brain networks to be described in a hypothesis-free, data-driven way by identifying patterns of covariation in the data. In contrast to alternative techniques, such as principal component analysis and independent component analysis, which yield components with both positive and negative weights that are often difficult to interpret, NNMF produces a sparse, positive-only, parts-based representation of the data. Importantly, NNMF has previously been proven effective in estimating covariance patterns in neuroimaging data while providing an easier interpretation of the results than other matrix decomposition techniques such as principal component analysis (PCA) or independent component analysis (ICA)[26-28,70,71].

Briefly, NNMF decomposes an input matrix (voxels×subjects) into two matrices; a component matrix W (voxels×k) and a weight matrix H (k×subjects) where *k* is the number of components that needs to be specified by the user. Here, we used an implementation of orthogolnal projective non-negative matrix factorization previously used in a number of publications[26-28,70,71] and downloaded from https://github.com/asotiras/brainparts. Given the large number of participants, we used the opnmf_mem.m function, which has been optimized for high-dimensional data. The function was run

with default parameter settings, exept for maximal number of iterations, which was increased to 200k, in order to ensure full convergence across all tested model orders.

Model order selection

Since the resulting parcellations are highly dependent on the requested number of components (or model order) specified, we tested model orders ranging from 2 to 30 in steps of 1, as well as from 30 to 100 in steps of 10. Binarized winner-winner-takes-all (i.e. assigning each voxel to the NNMF component with the highest loading) maps of the resulting decompositions projected onto a flattened representation of the cerebellar cortex are shown in Supplementary Figure 1.

Resulting NNMF decompositions were then evaluated based on two criteria; 1) how much of the variance in the original input data a given NNMF solution (i.e., component maps and subject weights) could explain and on 2) how reproducible the component maps were. As a metric of change in explained variance we used the change of the Frobenius norm of the reconstruction error. With increasing model orders the variance explained will always increase and the reconstruction error decrease, but if the decrease in the reconstruction error (or gradient) levels off, this indicates that the intrinsic dimensionality of the data might have been approximated (and that the subsequent increase in explained variance can largely be attributed to fitting random noise in the input data). In order to assess reproducibility, we split the full dataset into two equal sets (matched with respect to scanner site, n = 14,105 and 14,107, respectively), and ran NNMF on each split-half sample. For each set of independent NNMF parcellations, we computed two reproducibility indices. First, for each model order we matched components across split-half runs using the Hungarian algorithm[72], before computing the spatial correlations between matched component maps, and extracting the median correlation across all matched components as our first reproducibility index. For our second reproducibility index, we first computed one overall – and categorical – component map using a “winner-takes-all”-approach, i.e., assigning each voxel to the NNMF component with the highest loading. Next, we calculated the adjusted Rand index (ranging from 0 to 1, with higher values indicating greater similarity[73], across the two categorical parcellation maps for each model order as our second metric of reproducibility.

As can be seen in Supplementary Figure 2A, for lower model orders, increasing the model order resulted in a sharp decrease in the reconstruction error, indicating that models with more components resulted in a significantly better fit to the data. However, after reaching model orders between 15 and 30, the incremental improvement in fit from adding another component appeared to level off. As expected, the reproducibility results showed a largely inverse pattern, with both reproducibility indices decreasing with increasing model orders (Supplementary Figure 2B). Of note, for model orders up to 8, median spatial correlations across all matched components was above .99, indicating almost identical parcellations derived from the two independent samples. However, even for a model order of 100, the median pairwise correlation was still pretty high (.85), with 60% of components showing pairwise spatial correlations above 0.8, suggesting a reasonable level of

reproducibility even for the most fine-grained parcellation. Our reproducibility index for the categorical parcellations showed very similar results; the adjusted Rand index remained above .9 for model orders up to 8, and then decreased to 0.56 at a model order of 100.

Given that the change in reconstruction error appeared to stabilize between 15 and 30 components, indicating that the intrinsic dimensionality of the data had been approximated, we searched for the most reproducible parcellations within this range. Since the reliability estimates for model orders of 16 and 23 were very similar, with the 23-component solution explaining more of the variance in the original data, we used the 23-component parcellation for all further analyses.

Adjustment and rank-order normalization of anatomical indices

Prior to being subjected to genome-wide association analyses, we adjusted all anatomical indices for effects of age, sex, estimated total intracranial volume, scanner site, 40 genetic population components, genetic batch and mean Euler number (i.e, an index of MRI image quality[29], averaged across hemispheres). Finally, all adjusted anatomical indices were inverse rank normalized[74].

Pre-processing of genetic data

For all genetic analyses we made use of the UKB v3 imputed data, which has undergone extensive quality control procedures as described by the UKB genetics team[75]. After converting the BGEN format to PLINK binary format, we additionally carried out standard quality check procedures. We first selected White Europeans, as determined by a combination of self-identification as 'White British' and similar genetic ancestry based on genetic principal components, that had undergone the neuroimaging protocol. We then filtered out individuals with more than 10% missingness, removed SNPs with low imputation quality scores (INFO <.5), SNPs with more than 10% missingness, and SNPs failing the Hardy-Weinberg equilibrium test at p=1*10-9. We further set a minor allele frequency threshold of 0.005 leaving 9,061,238 SNPs. After estimating the genetic relationship matrix (GRM) using genetic complex trait analysis (GCTA[31]), we finally removed 910 participants defined as close relatives using a threshold of 0.05 (approximately corresponding to 3rd cousins).

Heritability estimation and genetic correlation analyses

SNP-based heritability estimates for all morphological features – as well as the pairwise genetic correlations between cerebellar features - were estimated using genetic complex trait analysis (GCTA[31]).

Univariate genome-wide association analyses

Univariate analyses of total cerebellar grey matter volume and the ten cerebral comparison phenotypes were conducted using Plink v1.9.

Genetic correlation analyses across discovery and replication samples and with previous published GWASs

Genetic correlation analyses across different samples were conducted using LD-score regression[30].

Multivariate genome-wide association analyses

For our main analysis, we used a recently developed multivariate analysis method (MOSTest[34]), to conduct a multivariate genome-wide association (GWA) analysis on cerebellar morphological features. MOSTest identifies genetic effects across multiple phenotypes, yielding a multivariate GWAS summary statistic across all 23 features, and provides robust (permutation based) test statistics. For mathematical details of the implementation, see van der Meer et al. (2020)[34], for details on the software implementation see github.com/precimed/mostest. MOSTest has been extensively validated in the original methods paper, including simulations and comparisons with other methods that have confirmed its solid discovery performance as well as an order of magnitude shorter runtime compared to other tools[34]. For comparison to standard univariate approaches, we also performed univariate GWASs (extracted from the univariate stream of MOSTest[34] and identical to results from analyses using Plink).

Multivariate replication analysis

To ensure that not only single lead SNP associations replicate but that also the multivariate pattern of these associations are consistent in the discovery and replication sample, we implemented a multivariate replication procedure established in Loughnan et al.[37]. In brief, for each lead SNP identified in the multivariate analysis in the discovery sample, this procedure derives a composite score from the mass-univariate *z*-statistics and tests for associations of the composite score with the genotype in the replication sample (for mathematical formulation see Loughnan et al.[37]). 19 of the 560 lead SNPs could not be tested as they were not available in the replication sample. For the remaining SNPs we report the percent of loci replicating at $P < 0.05$, the percent remaining significant after Bonferroni correction for 541 conducted tests, and the percent of lead SNPs showing the same effect direction. In addition, we report the percentage of genetic loci replicated (defined as containing at least one replicating lead SNP).

Multivariate cerebral comparison phenotypes

To compare key multivariate cerebellar results with other multivariate brain phenotypes, we downloaded summary statistics from two recent studies on cerebrocortical[45] and hippocampal[46] regional morphology. These comparison summary statistics were next analyzed using FUMA[35] as described for the main cerebellar results below.

Locus identification and SNP annotation

To identify genetic loci we uploaded summary statistics to the FUMA platform v1.4.1[35] Using the 1000GPhase3 EUR as reference panel, we identified independent SNPs as SNPs below the significance threshold of $P < 5e{-}8$ that were also in linkage equilibrium with each other at $r^2 < 0.6$. For each independent SNP, all candidate variants are identified as variants with LD r2≥ 0.6 with the independent SNP. A fraction of the independent significant SNPs in approximate linkage equilibrium with each other at $r^2 < 0.1$ were considered as lead SNPs. For a given lead SNP, the borders of the genomic locus are defined as min/max positional coordinates over all corresponding candidate SNPs. Finally, loci are merged if they are separated by less than 250kb.

FUMA further annotates associated SNPs based on functional categories, Combined Annotation Dependent Depletion (CADD) scores which predicts the deleteriousness of SNPs on protein structure/function[49], RegulomeDB scores which predicts regulatory functions[76]; and chromatin states that shows the transcription/regulation effects of chromatin states at the SNP locus[77]. For all these analyses, we used default FUMA parameters.

Genome-wide gene-based association and gene-set analyses

We conducted genome-wide gene-based association and gene-set analyses using MAGMA v.1.10[42] (http://ctg.cncr.nl/software/magma). MAGMA performs multiple linear regression to map the input SNPs to 19,190 protein coding genes and estimates the significance value of that gene. Genes were considered significant if the *P* value was <0.05 after Bonferroni correction for 19,190 genes. The same procedure was used for MAGMA analysis of summary statistics for the three multivariate cerebral comparison phenotypes (cerebrocortical thickness and surface area[45] and regional hippocampal volumes[46]).

MAGMA gene-level statistics were next used as input to gene-property and gene-set analyses in MAGMA. Gene-property analyses test for associations between tissue specific gene expression profiles and disease-gene associations. The gene-property analysis is based on the regression model: $Z \sim \beta_0 + E_t\beta_E + A\beta_A + B\beta_B + \epsilon$, where Z is a gene-based Z-score converted from the gene-based P-value, B is a matrix of several technical confounders included by default (e.g., gene size, gene density, sample size), E_t is the gene expression value of a testing tissue type and A is the average expression across all tissue types in a data set (ensuring a test of expression specificity). We performed a one-sided test ($\beta_E > 0$) which is essentially testing the positive relationship between tissue specificity and genetic association of genes.

We tested associations with two regional brain gene expression datasets (Allen Human Brain Atlas[33] and GTEx) and one developmental brain gene expression dataset (BrainSpan). For extraction and processing of gene expression data, see below.

Extraction and processing of gene expression data

Allen Human Brain Atlas: Regional microarray expression data were obtained from 6 post-mortem brains (1 female, ages 24.0--57.0, 42.50 +/- 13.38) provided by the Allen Human Brain Atlas[33]. Data were processed with the abagen toolbox (version 0.1.3) [32] using two volumetric atlases; 1) the binarized 23-region NNMF-derived parcellation of the cerebellar cortex; and 2) a modified version of the Desikan atlas were ROIs were merged to construct 9 bilateral regions: cerebellum, cerebral cortex, pallidum, caudate, putamen, thalamus, amygdala, nucleus accumbens and hippocampus.

First, microarray probes were reannotated using data provided by Arnatkeviciute, Fulcher and Fornito[78]; probes not matched to a valid Entrez ID were discarded. Next, probes were filtered based on their expression intensity relative to background noise[79], such that probes with intensity less than the background in >=50.00% of samples across donors were discarded, yielding 31,569 probes. When multiple probes indexed the expression of the same gene, we selected and used the probe with the most consistent pattern of regional variation across donors (i.e., differential stability[80]), calculated with:

$$\Delta_S(p) = \frac{1}{\binom{N}{2}} \sum_{i=1}^{N-1} \sum_{j=i+1}^{N} \rho[B_i(p), B_j(p)]$$

where *p* is Spearman's rank correlation of the expression of a single probe, p, across regions in two donors B_i and B_j, and N is the total number of donors.

Here, regions correspond to the structural designations provided in the ontology from the AHBA. The MNI coordinates of tissue samples were updated to those generated via non-linear registration using the Advanced Normalization Tools (ANTs; https://github.com/chrisfilo/alleninf). Samples were assigned to brain regions in the provided atlas if their MNI coordinates were within 2 mm of a given parcel. To reduce the potential for misassignment, sample-to-region matching was constrained by hemisphere and gross structural divisions (i.e., cortex, subcortex/ brainstem, and cerebellum, such that e.g., a sample in the left cortex could only be assigned to an atlas parcel in the left cortex[78]). All tissue samples not assigned to a brain region in the provided atlas were discarded. \n\nInter-subject variation was addressed by normalizing tissue sample expression values across genes using a robust sigmoid function[81]:

$$x_{norm} = \frac{1}{1+\exp(-\frac{(x-\langle x \rangle)}{\mathrm{IQR}_x})}$$

where (x) is the median and IQR_z is the normalized interquartile range of the expression of a single tissue sample across genes. Normalized expression values were then rescaled to the unit interval:

$$x_{scaled} = \frac{x_{norm} - \min(x_{norm})}{\max(x_{norm}) - \min(x_{norm})}$$

Gene expression values were then normalized across tissue samples using an identical procedure. Samples assigned to the same brain region were averaged separately for each donor and then across donors, yielding two regional expression matrices with 23 and 9 rows, corresponding to brain regions, and 15,631 and 15,633 columns, corresponding to the retained genes. Prior to inclusion in MAGMA gene property analyses, we converted gene names for the modified Desikan atlas to ENSMBL IDs, and calculated the mean expression value across tissue types (in order to include this as a covariate in MAGMA analyses testing for gene expression specificity), resulting in a 10 (regions) by (15,490) gene expression matrix.

GTeX: Text files containing median transcript per millimeter (TPM) values for 53 tissue types (GTEx_Analysis_2017-06-05_v8_RNASeQCv1.1.9_gene_median_tpm.gct.gz) were down-loaded from the GTEx portal (https://gtexportal.org/home/datasets/). After selecting only expression data from the seven (out of nine) comparison brain regions present in the GTEx dataset (i.e., amygdala, caudate, cerebellum, cortex, hippocampus, nucleus accumbens and putamen), we filtered the data by only including genes with median TPM values above 1 for at least one of these tissue type (retaining 19,578 of 56,200 annotated genes). Following the procedure used by FUMA[35], we next winsorized median TPM values at 50 (i.e., replaced TPM>50 with 50), before log transforming TPM with pseudocount 1 (log2(RPKM+1)). Finally, we calculated the mean expression value across tissue types (in order to include this as a covariate in MAGMA analyses testing for gene expression specificity).

BrainSpan data: The analysis of BrainSpan data testing for developmentally specific brain expression was performed entirely within FUMA v1.4.1., using default parameters.

Positional and eQTL mapping of SNPs to plausible causal genes

In addition to using MAGMA, we also mapped candidate SNPs to plausible causal genes using two complementary gene mapping strategies implemented ion FUMA[35]: 1) Positional mapping of deleterious SNPs (defined as having a CADD-score > 12.37) and 2) eQTL-mapping of SNPs previously shown to alter gene expression in cerebellar tissue (from the BRAINEAC and GTEx v8 databases). These analyses were run with default FUMA parameters. For the three multivariate cerebral comparison phenotypes (i.e., cerebrocortical thickness, cerebrocortical surface area and hippocampal regional volumes), we employed identical gene mapping procedures to our cerebellar morphology results, except for the tissues chosen for eQTL mapping (cerebrocortical and hippocampal, respectively).

Gene set analyses using lists of mapped genes

All gene set analyses using mapped genes were conducted using the hypeR R-package [82]. This package implements the hypergeometric test (also known as Fisher's exact test), which assigns a p-value to gene-set overlaps given gene set sizes and the number of background genes. This R-package also contains functions for downloading and/or formatting gene sets. The following gene sets were accessed using hypeR: "Allen_Brain_Atlas_up," "MGI_Mammalian_Phenotype_Level_4_2021", "DisGeNet" (all from the enrichR platform[83-85]), and "Gene ontology: Biological Proceses" (from the MsigDB platform[47,86,87]). In addition, we downloaded sets of genes with regional overexpression in the Allen Human Brain Atlas from the Harmonizome platform[88] and accessed a list of genes mapped to human accelerated regions[89]. For all gene-set analyses we employed Bonferroni-correction by dividing the p-value threshold of 0.05 by the number of gene sets included in each analysis.

Genetic overlap between cerebellar morphology and brain disorders

We accessed GWAS summary statistics for attention deficit hyperactivity disorder (ADHD)[90], autism spectrum disorder (ASD)[91], bipolar disorder (BIP)[92] and major depression (MD)[93] from the Psychiatric Genomics Consortium. Finally, we included data from a recent study of schizophrenia (SCZ)[94]. Shared variants associated with cerebellar morphology and each of the above-mentioned brain disorders were identified using conjunctional FDR statistics (FDR < 0.05)[95,96]. In contrast to genetic correlation analysis, conjunctional FDR does not require effect directions and can therefore be applied to summary statistics from multivariate GWAS, which do not contain effect directions. Two genomic regions, the extended major histocompatibility complex genes region (hg19 location Chr 6: 25119106–33854733) and chromosome 8p23.1 (hg19 location Chr 8: 7242715–12483982) for all cases and *APOE* region for ASD, were excluded from the FDR-fitting procedures because complex correlations in regions with intricate LD can bias FDR estimation. We submitted the results from conjunctional FDR to FUMA v1.3.7[35] to annotate the genomic loci with conjFDR value < 0.10 having an $r^2 \geq 0.6$ with one of the independent significant SNPs. Genetic correlations between univariate results for the 23 cerebellar features and each of the five mental disorders were computed using LD-score regression as described above.

References for Online Methods:

1. Herculano-Houzel, S. *The human advantage : a new understanding of how our brain became remarkable*, xiii, 256 pages (The MIT Press, Cambridge, Massachusetts, 2016).
2. Barton, R.A. & Venditti, C. Rapid Evolution of the Cerebellum in Humans and Other Great Apes. in *Curr. Biol.* (2014).
3. Sereno, M.I. *et al.* The human cerebellum has almost 80% of the surface area of the neocortex. *Proc Natl Acad Sci U S A* **117**, 19538-19543 (2020).
4. Harrison, P.W. & Montgomery, S.H. Genetics of Cerebellar and Neocortical Expansion in Anthropoid Primates: A Comparative Approach. *Brain Behav Evol* **89**, 274-285 (2017).
5. Leiner, H.C., Leiner, A.L. & Dow, R.S. Cognitive and language functions of the human cerebellum. in *Trends in Neurosciences* Vol. 16 444-447 (1993).
6. Strick, P.L., Dum, R.P. & Fiez, J.A. Cerebellum and Nonmotor Function. in *Annu. Rev. Neurosci.* Vol. 32 413-434 (2009).
7. Buckner, R.L. The cerebellum and cognitive function: 25 years of insight from anatomy and neuroimaging. in *Neuron* Vol. 80 807-815 (2013).
8. King, M., Hernandez-Castillo, C.R., Poldrack, R.A., Ivry, R.B. & Diedrichsen, J. Functional boundaries in the human cerebellum revealed by a multi-domain task battery. *Nat Neurosci* **22**, 1371-1378 (2019).
9. Wang, S.S., Kloth, A.D. & Badura, A. The cerebellum, sensitive periods, and autism. *Neuron* **83**, 518-32 (2014).
10. Moberget, T. *et al.* Cerebellar volume and cerebellocerebral structural covariance in schizophrenia: a multisite mega-analysis of 983 patients and 1349 healthy controls. *Mol Psychiatry* **23**, 1512-1520 (2018).
11. Adams, H.H. *et al.* Novel genetic loci underlying human intracranial volume identified through genome-wide association. *Nat Neurosci* **19**, 1569-1582 (2016).
12. van der Meer, D. *et al.* Brain scans from 21,297 individuals reveal the genetic architecture of hippocampal subfield volumes. *Mol Psychiatry* (2018).
13. Chambers, T. *et al.* Genetic common variants associated with cerebellar volume and their overlap with mental disorders: a study on 33,265 individuals from the UK-Biobank. *Mol Psychiatry* **27**, 2282-2290 (2022).
14. Tissink, E. *et al.* Genome-wide association study of cerebellar volume provides insights into heritable mechanisms underlying brain development and mental health. *Commun Biol* **5**, 710 (2022).
15. Macri, S., Savriama, Y., Khan, I. & Di-Poi, N. Comparative analysis of squamate brains unveils multi-level variation in cerebellar architecture associated with locomotor specialization. *Nat Commun* **10**, 5560 (2019).
16. Smaers, J.B., Turner, A.H., Gomez-Robles, A. & Sherwood, C.C. A cerebellar substrate for cognition evolved multiple times independently in mammals. *Elife* **7**(2018).
17. E, K.-H., Chen, S.-H.A., Ho, M.-H.R. & Desmond, J.E. A meta-analysis of cerebellar contributions to higher cognition from PET and fMRI studies. in *Hum Brain Mapp* Vol. 35 593-615 (2014).
18. Stoodley, C.J. & Schmahmann, J.D. Functional topography in the human cerebellum: a meta-analysis of neuroimaging studies. in *NeuroImage* Vol. 44 489-501 (2009).
19. Buckner, R.L., Krienen, F.M., Castellanos, A., Diaz, J.C. & Yeo, B.T.T. The organization of the human cerebellum estimated by intrinsic functional connectivity. in *Journal of Neurophysiology* Vol. 106 2322-2345 (2011).
20. Sang, L. *et al.* Resting-state functional connectivity of the vermal and hemispheric subregions of the cerebellum with both the cerebral cortical networks and subcortical structures. in *NeuroImage* Vol. 61 1213-1225 (Elsevier Inc., 2012).
21. Krienen, F.M. & Buckner, R.L. Segregated fronto-cerebellar circuits revealed by intrinsic functional connectivity. in *Cerebral Cortex* Vol. 19 2485-2497 (2009).

22. Bernard, J.A. *et al.* Resting state cortico-cerebellar functional connectivity networks: a comparison of anatomical and self-organizing map approaches. in *Front Neuroanat* Vol. 6 31 (2012).
23. Kipping, J.A. *et al.* Overlapping and parallel cerebello-cerebral networks contributing to sensorimotor control: an intrinsic functional connectivity study. in *NeuroImage* Vol. 83 837-848 (2013).
24. Wang, C., Kipping, J., Bao, C., Ji, H. & Qiu, A. Cerebellar Functional Parcellation Using Sparse Dictionary Learning Clustering. *Front Neurosci* **10**, 188 (2016).
25. Kipping, J.A., Tuan, T.A., Fortier, M.V. & Qiu, A. Asynchronous Development of Cerebellar, Cerebello-Cortical, and Cortico-Cortical Functional Networks in Infancy, Childhood, and Adulthood. *Cereb Cortex* (2016).
26. Sotiras, A., Resnick, S.M. & Davatzikos, C. Finding imaging patterns of structural covariance via Non-Negative Matrix Factorization. *Neuroimage* **108**, 1-16 (2015).
27. Sotiras, A. *et al.* Patterns of coordinated cortical remodeling during adolescence and their associations with functional specialization and evolutionary expansion. *Proc Natl Acad Sci U S A* **114**, 3527-3532 (2017).
28. Varikuti, D.P. *et al.* Evaluation of non-negative matrix factorization of grey matter in age prediction. *Neuroimage* **173**, 394-410 (2018).
29. Rosen, A.F.G. *et al.* Quantitative assessment of structural image quality. *Neuroimage* **169**, 407-418 (2018).
30. Bulik-Sullivan, B.K. *et al.* LD Score regression distinguishes confounding from polygenicity in genome-wide association studies. *Nat Genet* **47**, 291-5 (2015).
31. Yang, J., Lee, S.H., Goddard, M.E. & Visscher, P.M. GCTA: a tool for genome-wide complex trait analysis. *Am J Hum Genet* **88**, 76-82 (2011).
32. Markello, R.D. *et al.* Standardizing workflows in imaging transcriptomics with the abagen toolbox. *Elife* **10**(2021).
33. Hawrylycz, M.J. *et al.* An anatomically comprehensive atlas of the adult human brain transcriptome. *Nature* **489**, 391-399 (2012).
34. van der Meer, D. *et al.* Understanding the genetic determinants of the brain with MOSTest. *Nat Commun* **11**, 3512 (2020).
35. Watanabe, K., Taskesen, E., van Bochoven, A. & Posthuma, D. Functional mapping and annotation of genetic associations with FUMA. *Nat Commun* **8**, 1826 (2017).
36. Wang, K., Li, M. & Hakonarson, H. ANNOVAR: functional annotation of genetic variants from high-throughput sequencing data. *Nucleic Acids Res* **38**, e164 (2010).
37. Loughnan, R.J. *et al.* Generalization of cortical MOSTest genome-wide associations within and across samples. *Neuroimage* **263**, 119632 (2022).
38. van der Sluis, S., Posthuma, D. & Dolan, C.V. TATES: efficient multivariate genotype-phenotype analysis for genome-wide association studies. *PLoS Genet* **9**, e1003235 (2013).
39. O'Reilly, P.F. *et al.* MultiPhen: joint model of multiple phenotypes can increase discovery in GWAS. *PLoS One* **7**, e34861 (2012).
40. Zhao, B. *et al.* Genome-wide association analysis of 19,629 individuals identifies variants influencing regional brain volumes and refines their genetic co-architecture with cognitive and mental health traits. *Nat Genet* **51**, 1637-1644 (2019).
41. Smith, S.M. *et al.* An expanded set of genome-wide association studies of brain imaging phenotypes in UK Biobank. *Nat Neurosci* **24**, 737-745 (2021).
42. de Leeuw, C.A., Mooij, J.M., Heskes, T. & Posthuma, D. MAGMA: generalized gene-set analysis of GWAS data. *PLoS Comput Biol* **11**, e1004219 (2015).
43. Wei, Y. *et al.* Genetic mapping and evolutionary analysis of human-expanded cognitive networks. *Nat Commun* **10**, 4839 (2019).
44. Won, H., Huang, J., Opland, C.K., Hartl, C.L. & Geschwind, D.H. Human evolved regulatory elements modulate genes involved in cortical expansion and neurodevelopmental disease susceptibility. *Nat Commun* **10**, 2396 (2019).

45. van der Meer, D. *et al.* The genetic architecture of human cortical folding. *Sci Adv* **7**, eabj9446 (2021).
46. Bahrami, S. *et al.* Distributed genetic architecture across the hippocampal formation implies common neuropathology across brain disorders. *Nat Commun* **13**, 3436 (2022).
47. Liberzon, A. *et al.* The Molecular Signatures Database (MSigDB) hallmark gene set collection. *Cell Syst* **1**, 417-425 (2015).
48. Subramanian, A. *et al.* Gene set enrichment analysis: a knowledge-based approach for interpreting genome-wide expression profiles. *Proc Natl Acad Sci U S A* **102**, 15545-50 (2005).
49. Kircher, M. *et al.* A general framework for estimating the relative pathogenicity of human genetic variants. *Nat Genet* **46**, 310-5 (2014).
50. Andreassen, O.A. *et al.* Improved detection of common variants associated with schizophrenia and bipolar disorder using pleiotropy-informed conditional false discovery rate. *PLoS Genet* **9**, e1003455 (2013).
51. Guissart, C. *et al.* Dual Molecular Effects of Dominant RORA Mutations Cause Two Variants of Syndromic Intellectual Disability with Either Autism or Cerebellar Ataxia. *Am J Hum Genet* **102**, 744-759 (2018).
52. Chi, C.L., Martinez, S., Wurst, W. & Martin, G.R. The isthmic organizer signal FGF8 is required for cell survival in the prospective midbrain and cerebellum. *Development* **130**, 2633-44 (2003).
53. Li, S., Qiu, F., Xu, A., Price, S.M. & Xiang, M. Barhl1 regulates migration and survival of cerebellar granule cells by controlling expression of the neurotrophin-3 gene. *J Neurosci* **24**, 3104-14 (2004).
54. Valence, S. *et al.* RELN and VLDLR mutations underlie two distinguishable clinico-radiological phenotypes. *Clin Genet* **90**, 545-549 (2016).
55. Larouche, M., Beffert, U., Herz, J. & Hawkes, R. The Reelin receptors Apoer2 and Vldlr coordinate the patterning of Purkinje cell topography in the developing mouse cerebellum. *PLoS One* **3**, e1653 (2008).
56. Wolfers, T. *et al.* Mapping the Heterogeneous Phenotype of Schizophrenia and Bipolar Disorder Using Normative Models. *JAMA Psychiatry* **75**, 1146-1155 (2018).
57. Wolfers, T. *et al.* Replicating extensive brain structural heterogeneity in individuals with schizophrenia and bipolar disorder. *Hum Brain Mapp* **42**, 2546-2555 (2021).
58. Armstrong, N.C., Anderson, R.C. & McDermott, K.W. Reelin: Diverse roles in central nervous system development, health and disease. *Int J Biochem Cell Biol* **112**, 72-75 (2019).
59. Li, M. *et al.* Convergent Lines of Evidence Support LRP8 as a Susceptibility Gene for Psychosis. *Mol Neurobiol* **53**, 6608-6619 (2016).
60. King, M.Z., Zonglei; Ivry, Richard B.; Weiner, Kevin S. Transcriptomic Gradients Of The Human Cerebellum.
61. Guell, X., Gabrieli, J.D.E. & Schmahmann, J.D. Triple representation of language, working memory, social and emotion processing in the cerebellum: convergent evidence from task and seed-based resting-state fMRI analyses in a single large cohort. *Neuroimage* **172**, 437-449 (2018).
62. Chen, C.H. *et al.* Hierarchical genetic organization of human cortical surface area. *Science* **335**, 1634-6 (2012).
63. Chen, C.H. *et al.* Genetic topography of brain morphology. *Proc Natl Acad Sci U S A* **110**, 17089-94 (2013).
64. Fischl, B. *et al.* Whole brain segmentation: automated labeling of neuroanatomical structures in the human brain. *Neuron* **33**, 341-55 (2002).
65. Diedrichsen, J. A spatially unbiased atlas template of the human cerebellum. in *NeuroImage* Vol. 33 127-138 (2006).
66. Leys, C., Ley, C., Klein, O., Bernard, P. & Licata, L. Detecting outliers: Do not use standard deviation around the mean, use absolute deviation around the median. *Journal of Experimental Social Psychology* **49**, 764-766 (2013).
67. de Jong, L.W. *et al.* Allometric scaling of brain regions to intra-cranial volume: An epidemiological MRI study. *Hum Brain Mapp* **38**, 151-164 (2017).

68. Mankiw, C. *et al.* Allometric Analysis Detects Brain Size-Independent Effects of Sex and Sex Chromosome Complement on Human Cerebellar Organization. *J Neurosci* **37**, 5221-5231 (2017).
69. Friston, K.J. *Statistical parametric mapping : the analysis of funtional brain images*, vii, 647 p. (Elsevier/Academic Press, Amsterdam ; Boston, 2007).
70. Nassar, R. *et al.* Gestational Age is Dimensionally Associated with Structural Brain Network Abnormalities Across Development. *Cereb Cortex* **29**, 2102-2114 (2019).
71. Pehlivanova, M. *et al.* Diminished Cortical Thickness Is Associated with Impulsive Choice in Adolescence. *J Neurosci* **38**, 2471-2481 (2018).
72. Kuhn, H.W. The Hungarian method for the assignment problem. *Naval Research Logistics Quarterly* **2**, 14 (1955).
73. Santos, J.M. & Embrechts, M. On the Use of the Adjusted Rand Index as a Metric for Evaluating Supervised Classification. 175-184 (Springer Berlin Heidelberg, Berlin, Heidelberg, 2009).
74. Beasley, T.M., Erickson, S. & Allison, D.B. Rank-based inverse normal transformations are increasingly used, but are they merited? *Behav Genet* **39**, 580-95 (2009).
75. Bycroft, C. *et al.* The UK Biobank resource with deep phenotyping and genomic data. *Nature* **562**, 203-209 (2018).
76. Boyle, A.P. *et al.* Annotation of functional variation in personal genomes using RegulomeDB. *Genome Res* **22**, 1790-7 (2012).
77. Zhu, Z. *et al.* Integration of summary data from GWAS and eQTL studies predicts complex trait gene targets. *Nat Genet* **48**, 481-7 (2016).
78. Arnatkeviciute, A., Fulcher, B.D. & Fornito, A. A practical guide to linking brain-wide gene expression and neuroimaging data. *Neuroimage* **189**, 353-367 (2019).
79. Quackenbush, J. Microarray data normalization and transformation. *Nat Genet* **32 Suppl**, 496-501 (2002).
80. Hawrylycz, M. *et al.* Canonical genetic signatures of the adult human brain. *Nat Neurosci* **18**, 1832-44 (2015).
81. Fulcher, B.D., Little, M.A. & Jones, N.S. Highly comparative time-series analysis: the empirical structure of time series and their methods. *J R Soc Interface* **10**, 20130048 (2013).
82. Federico, A. & Monti, S. hypeR: an R package for geneset enrichment workflows. *Bioinformatics* **36**, 1307-1308 (2020).
83. Chen, E.Y. *et al.* Enrichr: interactive and collaborative HTML5 gene list enrichment analysis tool. *BMC Bioinformatics* **14**, 128 (2013).
84. Kuleshov, M.V. *et al.* Enrichr: a comprehensive gene set enrichment analysis web server 2016 update. *Nucleic Acids Res* **44**, W90-7 (2016).
85. Xie, Z. *et al.* Gene Set Knowledge Discovery with Enrichr. *Curr Protoc* **1**, e90 (2021).
86. Liberzon, A. A description of the Molecular Signatures Database (MSigDB) Web site. *Methods Mol Biol* **1150**, 153-60 (2014).
87. Liberzon, A. *et al.* Molecular signatures database (MSigDB) 3.0. *Bioinformatics* **27**, 1739-40 (2011).
88. Rouillard, A.D. *et al.* The harmonizome: a collection of processed datasets gathered to serve and mine knowledge about genes and proteins. *Database (Oxford)* **2016**(2016).
89. Doan, R.N. *et al.* Mutations in Human Accelerated Regions Disrupt Cognition and Social Behavior. *Cell* **167**, 341-354 e12 (2016).
90. Demontis, D. *et al.* Discovery of the first genome-wide significant risk loci for attention deficit/hyperactivity disorder. *Nat Genet* **51**, 63-75 (2019).
91. Grove, J. *et al.* Identification of common genetic risk variants for autism spectrum disorder. *Nat Genet* **51**, 431-444 (2019).
92. Mullins, N. *et al.* Genome-wide association study of more than 40,000 bipolar disorder cases provides new insights into the underlying biology. *Nat Genet* **53**, 817-829 (2021).
93. Wray, N.R. *et al.* Genome-wide association analyses identify 44 risk variants and refine the genetic architecture of major depression. *Nat Genet* **50**, 668-681 (2018).

94. Pardinas, A.F. *et al.* Common schizophrenia alleles are enriched in mutation-intolerant genes and in regions under strong background selection. *Nat Genet* **50**, 381-389 (2018).
95. Andreassen, O.A. *et al.* Improved detection of common variants associated with schizophrenia by leveraging pleiotropy with cardiovascular-disease risk factors. *Am J Hum Genet* **92**, 197-209 (2013).
96. Smeland, O.B. *et al.* Discovery of shared genomic loci using the conditional false discovery rate approach. *Hum Genet* **139**, 85-94 (2020).